

# Self-Consistent and Efficient Treatment of Relativistic Effects with Periodic Density Functional Methods: Energies, Gradients, and Stress Tensors

Yannick J. Franzke,<sup>1</sup> Werner M. Schosser,<sup>2</sup> and Fabian Pauly<sup>2,\*</sup>

<sup>1</sup>*Fachbereich Chemie, Philipps-Universität Marburg,  
Hans-Meerwein-Str. 4, 35032 Marburg, Germany*<sup>†</sup>

<sup>2</sup>*Institute of Physics and Centre for Advanced Analytics and Predictive Sciences,  
University of Augsburg, Universitätsstr. 1, 86159 Augsburg, Germany*<sup>‡</sup>

(Dated: May 9, 2023)

The implementation of an efficient self-consistent field (SCF) method including both scalar relativistic effects and spin-orbit interaction in density functional theory (DFT) is presented. We make use of Gaussian-type orbitals (GTOs) and all integrals are evaluated in real space. Therefore, this implementation is able to treat molecular and periodic systems of any dimensionality on an equal footing up to the level of *meta*-generalized gradient approximations (mGGAs) for SCF energies and gradients. The latter can be used to compute the stress tensor and consequently allow us to optimize the cell structure. Considering spin-orbit interaction requires the extension of the standard procedures to a two-component (2c) formalism. That is, a non-collinear DFT formalism is needed for open-shell systems. We demonstrate both efficiency and the relevance of spin-orbit effects for the electronic structure of periodic systems of one to three dimensions.

## I. INTRODUCTION

Modern physics, chemistry, and materials science rely on the theories of quantum mechanics and of special relativity. Particularly for systems that include elements with high nuclear charge, the interplay between both theories is crucial [1–13]. The occurring relativistic effects can be divided into two categories, scalar-relativistic (spin-independent) and spin-dependent relativistic effects. The most prominent scalar-relativistic effects are the energy-momentum or the mass-velocity relation and the Darwin term, which describes the electrostatic interaction between electrons and the field of the nuclei. The dominating spin-dependent relativistic effect is the interaction between the electron's spin and its orbital momentum. For lighter elements, this correction is of negligible or small size and may be treated with spin-orbit perturbation theory. However, for heavy *d* and *p* elements, such as platinum, gold, and lead [9, 14–16], it is of comparable size as scalar-relativistic effects and thus becomes relevant. Then, a self-consistent or variational ansatz treating both relativistic effects on an equal footing is necessary.

Spin-dependent relativistic effects are important for solids, low-dimensional systems, and surface science [17–19]. They are exploited in the field of spin-dependent quantum transport for magnetoresistive effects [20–27], for magnetic excitations such as skyrmions [28] caused by the Dzyaloshinskii-Moriya interaction [29, 30], and they may lead to spin-polarized surface states of topological insulators [31, 32].

Both scalar-relativistic and spin-orbit effects are efficiently modeled by effective core potentials (ECPs) [1, 33, 34]. Here, the core electrons are replaced with

pseudopotentials, which are fitted to high-level relativistic theories. This way, only the one-electron potential operator is directly affected. Therefore, scalar-relativistic effects can be incorporated at essentially no computational burden, as the electron-electron interaction operators are unaffected. However, the description of spin-orbit coupling requires a generalization of the framework. Due to the breakdown of spin symmetry and the complex form of the spin-orbit pseudopotentials or operators, a so-called 2c formalism employing complex algebra in real space is needed, which leads to an increase of the computational demands [35–42].

Offering relatively low computational costs combined with good accuracy, DFT is one of the most important computational tools concerning electronic structure theory. For periodic systems, scalar DFT approaches for energies and gradients are widely available in both plane-wave and GTO codes [43]. For instance, the TURBO-MOLE [44–47] program suite offers an efficient and stable program in order to perform these kinds of calculations for molecular and periodic systems, employing GTOs and fast multipole approximations combined with density fitting to ensure time efficiency. However, the functionalities to self-consistently include spin-orbit interaction for periodic systems are still missing in many program suites, preventing the simulation of promising relativistic systems. Especially open-shell systems require further modifications. That is, a non-collinear formulation of the exchange-correlation potential is needed [35–42]. Moreover, time-reversal symmetry does not hold anymore, see, e.g., Ref. [48]. In contrast, time-reversal symmetry and Kramers' theorem apply for closed-shell systems, which results in considerable simplifications for the exchange-correlation potential.

So far, a GTO-based non-collinear 2c DFT implementation for periodic systems and SCF energies was only presented by the group of Erba in the CRYSTAL package [48–51]. Density functional approximations up to the level of (hybrid) generalized gradient approximations

\* fabian.pauly@uni-a.de

<sup>†</sup> Y.J.F. and W.M.S. contributed equally to this work

(GGAs) are considered in their work. However, a corresponding implementation of 2c energy gradients has not been presented yet, at least to the best of our knowledge. Additionally, *meta*-generalized gradient approximations (mGGAs) may be superior to GGAs in terms of accuracy [52–64].

Therefore, our work aims to further fill this gap by introducing a 2c formalism to enable simulations of systems with periodic boundary conditions in DFT up to the level of *meta*-generalized gradient approximations including relativistic effects for energies, band structures, energy gradients, and the stress tensor to allow for structure optimizations. For this purpose, existing functionalities for relativistic calculations of molecular systems with a 2c formalism [37–39] will be introduced into TURBOMOLE’s RIPER module [65–71] and appropriately adapted.

## II. THEORY AND IMPLEMENTATION

In this section, we extend the 2c DFT formalism of Armbruster *et al.* [37, 38] to periodic systems [65–69]. Furthermore, the computational demands are assessed and compared to standard one-component (1c) procedures.

### A. Two-Component SCF Formalism

The 2c DFT formalism for periodic systems is based on the quasi-relativistic Hamiltonian in the Born–Oppenheimer approximation

$$H^{\vec{L}} = \sum_{i=1}^n \left[ \sigma_0 h_i^{0,\vec{L}} + \vec{\sigma} \cdot \vec{h}_i^{\text{SO},\vec{L}} \right] + V_{\text{ee}}^{\vec{L}} + V_{\text{NN}}^{\vec{L}} \quad (1)$$

for a unit cell (UC)  $\vec{L}$  and  $n$  electrons. The terms in the Hamiltonian include an effective spin–orbit (SO) operator,  $\vec{\sigma} \cdot \vec{h}_i^{\text{SO},\vec{L}}$ , that consists of the standard  $(2 \times 2)$  Pauli matrices  $\sigma_j$  ( $j = x, y, z$ ) and the vector operator  $\vec{h}_i^{\text{SO},\vec{L}}$ , which is a product of the orbital momentum and parameters fitted to results of, e.g., a relativistic four-component (4c) treatment [1, 33, 34]. Hence, the operators  $\vec{h}_i^{\text{SO},\vec{L}}$  lead to antisymmetric integrals in real space. Further, a spin-independent one-particle Hamiltonian  $h_i^0$  that describes the kinetic energy of the electrons and their potential energy in the field of the nuclei is included.  $\sigma_0$  is the identity matrix, whereas  $V_{\text{ee}}^{\vec{L}}$  and  $V_{\text{NN}}^{\vec{L}}$  represent the electron–electron interactions and the repulsion of the nuclei. Additionally, Grimme’s DFT dispersion corrections can be handled like the nuclear repulsion operator [72, 73]. We stress that the presence of the spin–orbit operator  $\vec{\sigma} \cdot \vec{h}_i^{\text{SO},\vec{L}}$  causes the spin not to be a conserved quantity anymore, i.e. the spin is not a ‘good’ quantum number.

The orbital wave functions  $\vec{\psi}_i^{\vec{k}}$  thus have to be adjusted. Due to the translational symmetry of solids, they

are a linear combination of Bloch–functions

$$\phi_{\mu}^{\vec{k}}(\vec{r}) = \frac{1}{\sqrt{N_{\text{UC}}}} \sum_{\vec{L}} e^{i\vec{k} \cdot \vec{L}} \xi_{\mu}^{\vec{L}}(\vec{r}) \quad (2)$$

that are expanded in terms of real-valued GTO basis functions

$$\xi_{\mu}^{\vec{L}}(\vec{r}) = \xi_{\mu}(\vec{r} - \vec{R}_{\mu} - \vec{L}), \quad (3)$$

centered at the atomic position  $\vec{R}_{\mu}$  in direct lattice cell  $\vec{L}$  over all  $N_{\text{UC}}$  unit cells. The wave functions are so-called 2c spinors

$$\vec{\psi}_i^{\vec{k}}(\vec{r}) = \sum_{\mu} \begin{pmatrix} c_{\mu i}^{\alpha,\vec{k}} \\ c_{\mu i}^{\beta,\vec{k}} \end{pmatrix} \phi_{\mu}^{\vec{k}}(\vec{r}) = \begin{pmatrix} \psi_i^{\alpha,\vec{k}}(\vec{r}) \\ \psi_i^{\beta,\vec{k}}(\vec{r}) \end{pmatrix} \quad (4)$$

with the spin indices  $\alpha$  and  $\beta$ , and complex coefficients  $c_{\mu i}^{\sigma,\vec{k}}$ . The spinors depend on the wave vector  $\vec{k}$  within the unit cell in reciprocal space, called the first Brillouin zone (FBZ), and the band index  $i$ .

Using this basis set expansion, the generalized Kohn–Sham (GKS) equations become

$$\begin{pmatrix} \mathbf{F}^{\alpha\alpha,\vec{k}} & \mathbf{F}^{\alpha\beta,\vec{k}} \\ \mathbf{F}^{\beta\alpha,\vec{k}} & \mathbf{F}^{\beta\beta,\vec{k}} \end{pmatrix} \begin{pmatrix} \mathbf{C}^{\alpha,\vec{k}} \\ \mathbf{C}^{\beta,\vec{k}} \end{pmatrix} = \begin{pmatrix} \mathbf{S}^{\vec{k}} & \mathbf{0} \\ \mathbf{0} & \mathbf{S}^{\vec{k}} \end{pmatrix} \begin{pmatrix} \mathbf{C}^{\alpha,\vec{k}} \\ \mathbf{C}^{\beta,\vec{k}} \end{pmatrix} \boldsymbol{\epsilon}^{\vec{k}} \quad (5)$$

with doubled dimension compared to the standard Kohn–Sham formulation. Here,  $\mathbf{F}$  is the Kohn–Sham–Fock matrix,  $\mathbf{C}^{\sigma,\vec{k}}$  is the matrix of the spinor coefficients  $c_{\mu i}^{\sigma,\vec{k}}$ , and  $\boldsymbol{\epsilon}^{\vec{k}}$  is the diagonal matrix of the spinor eigenvalues  $\epsilon_i^{\sigma,\vec{k}}$ . These Roothaan–Hall-like equations can be solved for each  $\vec{k}$  point separately in the FBZ. Both the overlap matrix between the GTOs

$$\mathbf{S}_{\mu\nu}^{\vec{k}} = \sum_{\vec{L}} e^{i\vec{k} \cdot \vec{L}} \mathbf{S}_{\mu\nu}^{\vec{L}} \quad (6)$$

with

$$\mathbf{S}_{\mu\nu}^{\vec{L}} = \mathbf{S}_{\mu\nu}^{\vec{0}\vec{L}} = \int \xi_{\mu}^{\vec{0}}(\vec{r}) \xi_{\nu}^{\vec{0}}(\vec{r}) d^3r \quad (7)$$

and the Kohn–Sham–Fock matrix

$$\mathbf{F}_{\mu\nu}^{\vec{k}} = \sum_{\vec{L}} e^{i\vec{k} \cdot \vec{L}} \mathbf{F}_{\mu\nu}^{\vec{L}} \quad (8)$$

are obtained via a Fourier transformation of the real space matrices. Following Eq. (1), the Kohn–Sham matrix components are [37]

$$\mathbf{F}_{\mu\nu}^{\alpha\alpha,\vec{L}} = T_{\mu\nu}^{\vec{L}} + J_{\mu\nu}^{\vec{L}} + h_{\mu\nu}^{z,\vec{L}} + X_{\mu\nu}^{\alpha\alpha,\vec{L}}, \quad (9)$$

$$\mathbf{F}_{\mu\nu}^{\alpha\beta,\vec{L}} = h_{\mu\nu}^{x,\vec{L}} - i h_{\mu\nu}^{y,\vec{L}} + X_{\mu\nu}^{\alpha\beta,\vec{L}}, \quad (10)$$

$$\mathbf{F}_{\mu\nu}^{\beta\beta,\vec{L}} = T_{\mu\nu}^{\vec{L}} + J_{\mu\nu}^{\vec{L}} - h_{\mu\nu}^{z,\vec{L}} + X_{\mu\nu}^{\beta\beta,\vec{L}}, \quad (11)$$

consisting of the kinetic energy matrix elements  $T_{\mu\nu}^{\vec{L}}$ , the Coulomb matrix elements  $J_{\mu\nu}^{\vec{L}}$ , the exchange–correlation (XC) matrix elements  $X_{\mu\nu}^{\sigma\sigma',\vec{L}}$  (with  $\sigma$  and  $\sigma'$  being the

spin indices), and the spin-orbit matrix elements  $h_{\mu\nu}^{j,\vec{L}}$  ( $j = x, y, z$ ). Thus, the total energy follows

$$E_{\text{SCF}} = E_{\text{T}} + E_{\text{J}} + E_{\text{SO}} + E_{\text{XC}} + E_{\text{NN}} \quad (12)$$

with the nuclear repulsion term  $E_{\text{NN}}$ . Note that the scalar ECP contribution  $h^{0,\vec{L}}$  is included in the kinetic energy matrix (see below). Spin-orbit coupling may lead to a breakdown of time-reversal symmetry, and therefore the Kohn–Sham equations generally need to be solved for  $+\vec{k}$  and  $-\vec{k}$  explicitly for systems without space-inversion symmetry [48]. Here, the full breakdown of time-reversal symmetry in momentum space is reached with hybrid functionals [48] or current density functionals [39].

In this 2c formalism, the general density matrix reads

$$\begin{aligned} \rho(\vec{r}, \vec{r}') &= \frac{1}{V_{\text{FBZ}}} \sum_{i=1}^n \int_{\text{FBZ}}^{\epsilon_i^{\vec{k}} < \epsilon_{\text{F}}} \vec{\psi}_{i\vec{k}}(\vec{r}) \left( \vec{\psi}_{i\vec{k}}(\vec{r}') \right)^\dagger d^3k \\ &= \begin{pmatrix} \rho^{\alpha\alpha}(\vec{r}, \vec{r}') & \rho^{\alpha\beta}(\vec{r}, \vec{r}') \\ \rho^{\beta\alpha}(\vec{r}, \vec{r}') & \rho^{\beta\beta}(\vec{r}, \vec{r}') \end{pmatrix}. \end{aligned} \quad (13)$$

It involves an integral over the FBZ,  $V_{\text{FBZ}}$  denotes the volume of the FBZ, and  $\epsilon_{\text{F}}$  is the Fermi level. The density matrix not only contains the particle density matrix

$$\rho_{\text{p}}(\vec{r}, \vec{r}') = \text{tr}[\rho(\vec{r}, \vec{r}')] = \sum_{\vec{L}} \text{tr}[\rho^{\vec{L}}(\vec{r}, \vec{r}')] \quad (14)$$

but also the spin-vector density matrix

$$\vec{\rho}_{\text{m}}(\vec{r}, \vec{r}') = \text{tr}[\vec{\sigma}\rho(\vec{r}, \vec{r}')] = \sum_{\vec{L}} \text{tr}[\vec{\sigma}\rho^{\vec{L}}(\vec{r}, \vec{r}')] \quad (15)$$

in terms  $N_{\text{UC}}$  unit-cell contributions associated with the lattice vectors  $\vec{L}$ , c.f. Eqs. (2) and (3). For easy handling within the program structure, the density matrix  $\rho_{\text{p}}(\vec{r}, \vec{r}')$  can be divided into the four spin contributions according to

$$\rho^{\sigma\sigma'}(\vec{r}, \vec{r}') = \sum_{\vec{L}} \rho^{\sigma\sigma',\vec{L}}(\vec{r}, \vec{r}'), \quad (16)$$

$$\rho^{\sigma\sigma',\vec{L}}(\vec{r}, \vec{r}') = \sum_{\mu\nu} \sum_{\vec{L}'} D_{\mu\nu}^{\sigma\sigma',-\vec{L}'} \xi_{\mu}^{\vec{L}}(\vec{r}) \xi_{\nu}^{\vec{L}'+\vec{L}}(\vec{r}'). \quad (17)$$

Thus, the electron density  $\rho^{\sigma\sigma'}(\vec{r})$  can be obtained with the atomic-orbital (AO) real space density matrix

$$D_{\mu\nu}^{\sigma\sigma',\vec{L}} = \frac{1}{V_{\text{FBZ}}} \sum_{i=1}^n \int_{\text{FBZ}}^{\epsilon_i^{\vec{k}} < \epsilon_{\text{F}}} e^{i\vec{k}\cdot\vec{L}} \left( c_{\mu i}^{\sigma,\vec{k}} c_{\nu i}^{*\sigma',\vec{k}} \right) d^3k \quad (18)$$

with the shorthand notation  $D_{\mu\nu}^{\sigma\sigma',\vec{L}} = D_{\mu\nu}^{\sigma\sigma',\vec{L}\vec{0}}$ . Note that the AO density matrix is a complex quantity in the 2c formalism and consists of eight blocks, i.e. four real and four imaginary spin blocks. The particle density,  $\rho_{\text{p}}(\vec{r}) = \rho_{\text{p}}(\vec{r}, \vec{r})$ , relates to the electron number  $n$  via

$$\int \rho_{\text{p}}(\vec{r}) d^3r = n, \quad (19)$$

while the spin-vector density or spin magnetization vector,  $\vec{\rho}_{\text{m}}(\vec{r}) = \vec{\rho}_{\text{m}}(\vec{r}, \vec{r})$ , is related to the expectation value of the system's spin according to

$$\langle \vec{S} \rangle = \frac{1}{2} \int \vec{\rho}_{\text{m}}(\vec{r}) d^3r. \quad (20)$$

In the absence of spin-orbit coupling, this is simply half the number of unpaired or spin-polarized electrons.

Evaluation of the kinetic term

$$T_{\mu\nu}^{\vec{L}} = \int \xi_{\mu}^{\vec{0}}(\vec{r}) \left[ -\frac{\nabla^2}{2} + V_{\text{sr}}^{\text{ECP}}(\vec{r}) \right] \xi_{\nu}^{\vec{L}}(\vec{r}) d^3r, \quad (21)$$

that also includes scalar relativistic energy corrections, employing the ECPs  $V_{\text{sr}}^{\text{ECP}}$ , needs no further modification compared to the 1c case, i.e. the elements  $T_{\mu\nu}^{\vec{L}}$  form a 1c matrix. Therefore, the respective energy is obtained as

$$\begin{aligned} E_{\text{T}} &= \sum_{\vec{L}} \int \left[ \mathbf{T}^{\vec{L}} \rho^{\vec{L}}(\vec{r}, \vec{r}') \right]_{\vec{r}=\vec{r}'} d^3r \\ &= \sum_{\mu\nu} \sum_{\vec{L}} T_{\mu\nu}^{\vec{L}} \left[ \text{Re}(D_{\nu\mu}^{\alpha\alpha,\vec{L}}) + \text{Re}(D_{\nu\mu}^{\beta\beta,\vec{L}}) \right]. \end{aligned} \quad (22)$$

The evaluation of the Coulomb interaction

$$J_{\mu\nu}^{\vec{L}} = \int \xi_{\mu}^{\vec{0}}(\vec{r}) \frac{\rho_{\text{p}}(\vec{r}') - \rho_{\text{N}}(\vec{r}')}{|\vec{r} - \vec{r}'|} \xi_{\nu}^{\vec{L}}(\vec{r}) d^3r d^3r' \quad (23)$$

utilizes a hierarchical scheme and density fitting [65] with the particle density  $\rho_{\text{p}}$  and the charge distribution  $\rho_{\text{N}}(\vec{r})$ . The latter is also written as a sum of UC contributions according to

$$\rho_{\text{N}}(\vec{r}) = \sum_{\vec{L}} \rho_{\text{N}}(\vec{r})^{\vec{L}}, \quad (24)$$

$$\rho_{\text{N}}(\vec{r})^{\vec{L}} = \sum_I Z_I^{\text{eff}} \delta(\vec{r} - \vec{R}_I - \vec{L}), \quad (25)$$

with the effective charges  $Z_I^{\text{eff}}$  and positions  $\vec{R}_I$  of the nuclei  $I$  in the reference cell. The 2c implementation of  $J_{\mu\nu}^{\vec{L}}$  is straightforward based on the 1c Kohn–Sham scheme, as the Coulomb interaction is independent of the spin and only depends on the particle density. The elements  $J_{\mu\nu}^{\vec{L}}$  hence form a 1c matrix. We refer to Refs. [65, 67] for details on the Coulomb matrix and the corresponding energy. Here, we just state that the Coulomb integrals are split into a crystal near field (CNF) and a crystal far field (CFF) contribution, yielding the following two contributions to the Coulomb energy

$$E_{\text{J}} = E_{\text{J,CNF}} + E_{\text{J,CFF}}. \quad (26)$$

As the first new terms compared to the 1c formalism, the spin-orbit ECP (SOECP) terms  $h_{\mu\nu}^{x,\vec{L}}$ ,  $h_{\mu\nu}^{y,\vec{L}}$ , and  $h_{\mu\nu}^{z,\vec{L}}$  are taken into account. They read

$$\begin{aligned} \mathbf{h}_{\mu\nu}^{\text{SO},\vec{L}} &= \begin{pmatrix} h_{\mu\nu}^{z,\vec{L}} & h_{\mu\nu}^{x,\vec{L}} - ih_{\mu\nu}^{y,\vec{L}} \\ h_{\mu\nu}^{x,\vec{L}} + ih_{\mu\nu}^{y,\vec{L}} & -h_{\mu\nu}^{z,\vec{L}} \end{pmatrix} \\ &= \int \xi_{\mu}^{\vec{0}}(\vec{r}) \mathbf{V}_{\text{SO}}^{\text{ECP}}(\vec{r}) \xi_{\nu}^{\vec{L}}(\vec{r}) d^3r \end{aligned} \quad (27)$$

with the effective spin-orbit potential  $\mathbf{V}_{\text{SO}}^{\text{ECP}}(\vec{r})$ . The associated spin-orbit energy is obtained as

$$E_{\text{SO}} = \sum_{\vec{L}} \int \left[ \vec{h}^{\text{SO},\vec{L}} \cdot \vec{\rho}_{\text{m}}^{\vec{L}}(\vec{r}, \vec{r}') \right]_{\vec{r}=\vec{r}'} d^3r. \quad (28)$$

Therefore, the antisymmetric linear combinations of the AO density matrices are needed, i.e.  $\text{Im}(D_{\nu\mu}^{\alpha\beta,\vec{L}}) + \text{Im}(D_{\nu\mu}^{\beta\alpha,\vec{L}})$ ,  $\text{Re}(D_{\nu\mu}^{\alpha\beta,\vec{L}}) - \text{Re}(D_{\nu\mu}^{\beta\alpha,\vec{L}})$ , and  $\text{Im}(D_{\nu\mu}^{\alpha\alpha,\vec{L}}) - \text{Im}(D_{\nu\mu}^{\beta\beta,\vec{L}})$  for the spin-orbit  $x$ ,  $y$ , and  $z$  components, respectively.

The final term, that has to be considered, involves the exchange-correlation matrices  $\mathbf{X}^{\sigma\sigma'}$ . They not only depend on the particle-number density  $\rho_{\text{p}}$  but also on the spin-vector density or spin magnetization vector  $\vec{\rho}_{\text{m}}$ . In the non-collinear formalism, the XC potential operator is given by

$$\begin{aligned} \mathbf{V}^{\text{XC}}[\rho_{\text{p}}(\vec{r}), |\vec{\rho}_{\text{m}}(\vec{r})|] &= \frac{\delta E_{\text{XC}}}{\delta \rho_{\text{p}}(\vec{r})} \sigma_0 + \sum_{u=\{x,y,z\}} \frac{\delta E_{\text{XC}}}{\delta \rho_{\text{m},u}(\vec{r})} \sigma_u \\ &= \frac{\delta E_{\text{XC}}}{\delta \rho_{\text{p}}(\vec{r})} \sigma_0 + \frac{\delta E_{\text{XC}}}{\delta |\vec{\rho}_{\text{m}}(\vec{r})|} \frac{\vec{\rho}_{\text{m}}(\vec{r}) \cdot \vec{\sigma}}{|\vec{\rho}_{\text{m}}(\vec{r})|}. \end{aligned} \quad (29)$$

It is based on the exchange-correlation energy as a functional of the particle density and the norm of the spin-vector density

$$E_{\text{XC}} = E_{\text{XC}}[\rho_{\text{p}}(\vec{r}), |\vec{\rho}_{\text{m}}(\vec{r})|] = E_{\text{XC}}[\rho_{\uparrow,\downarrow}(\vec{r})], \quad (30)$$

$$\rho_{\uparrow,\downarrow}(\vec{r}) = \frac{1}{2} [\rho_{\text{p}}(\vec{r}) \pm |\vec{\rho}_{\text{m}}(\vec{r})|]. \quad (31)$$

The XC energy for a given density functional approximation  $f^{\text{XC}}$  reads

$$E_{\text{XC}}[\rho_{\uparrow,\downarrow}(\vec{r})] = \int_{\text{UC}} f^{\text{XC}}[\rho_{\uparrow,\downarrow}(\vec{r}), \gamma_{\uparrow\uparrow,\uparrow\downarrow,\downarrow\downarrow}(\vec{r}), \tau_{\uparrow,\downarrow}(\vec{r})] d^3r, \quad (32)$$

using the auxiliary variable  $\gamma_{\sigma\sigma'} = \frac{1}{4}(\vec{\nabla}\rho_{\sigma}) \cdot (\vec{\nabla}\rho_{\sigma'})$  with  $\sigma, \sigma' \in \{\uparrow, \downarrow\}$  and the kinetic energy density  $\tau$  for *meta*-generalized gradient approximations. The kinetic energy density matrix may be defined analogously to the electron density as

$$\boldsymbol{\tau}(\vec{r}, \vec{r}') = \frac{1}{V_{\text{FBZ}}} \sum_{i=1}^n \int_{\text{FBZ}}^{\epsilon_i^{\vec{k}} < \epsilon_{\text{F}}} (\vec{\nabla}\psi_i^{\vec{k}}(\vec{r})) (\vec{\nabla}\psi_i^{\vec{k}}(\vec{r}'))^{\dagger} d^3k. \quad (33)$$

The particle kinetic energy density and the spin contributions then follow as

$$\tau_{\text{p}}(\vec{r}) = \text{tr}[\boldsymbol{\tau}(\vec{r})] = \text{tr}[\boldsymbol{\tau}(\vec{r}, \vec{r})], \quad (34)$$

$$\vec{\tau}_{\text{m}}(\vec{r}) = \text{tr}[\vec{\sigma}\boldsymbol{\tau}(\vec{r})], = \text{tr}[\vec{\sigma}\boldsymbol{\tau}(\vec{r}, \vec{r})], \quad (35)$$

which allows to construct  $\tau_{\uparrow,\downarrow}(\vec{r})$  analogously to Eq. (31). We note that the current density correction [39] for  $\boldsymbol{\tau}(\vec{r}, \vec{r}')$  is presently neglected in RIPER. Therefore, only the real and symmetric part of the spin magnetization in direct space is needed for the XC contribution, i.e.

$$\rho_{\text{m}}^x(\vec{r}) = \rho^{\alpha\beta}(\vec{r}) + \rho^{\beta\alpha}(\vec{r}), \quad (36)$$

$$\rho_{\text{m}}^y(\vec{r}) = i(\rho^{\alpha\beta}(\vec{r}) - \rho^{\beta\alpha}(\vec{r})), \quad (37)$$

$$\rho_{\text{m}}^z(\vec{r}) = \rho^{\alpha\alpha}(\vec{r}) - \rho^{\beta\beta}(\vec{r}). \quad (38)$$

In terms of AO density matrices, we need the symmetric linear combinations  $\text{Re}(D_{\nu\mu}^{\alpha\beta,\vec{L}}) + \text{Re}(D_{\nu\mu}^{\beta\alpha,\vec{L}})$ ,  $\text{Im}(D_{\nu\mu}^{\alpha\beta,\vec{L}}) - \text{Im}(D_{\nu\mu}^{\beta\alpha,\vec{L}})$ , and  $\text{Re}(D_{\nu\mu}^{\alpha\alpha,\vec{L}}) - \text{Re}(D_{\nu\mu}^{\beta\beta,\vec{L}})$  for the non-collinear  $x$ ,  $y$ , and  $z$  components.

For an implementation with real AO basis functions, it is advantageous to directly calculate the exchange-correlation potential in a matrix representation as

$$\mathbf{X}_{\mu\nu}^{\vec{L}} = \int \xi_{\mu}^{\vec{0}}(\vec{r}) \mathbf{V}^{\text{XC}}(\vec{r}) \xi_{\nu}^{\vec{L}}(\vec{r}) d^3r \quad (39)$$

by differentiation of the exchange-correlation energy with respect to the corresponding AO density matrices [74]. Thus, the quantities for the 2c formalism follow as

$$\begin{aligned} X_{\mu\nu,0}^{\vec{L}} &= \int \left[ \frac{\partial f^{\text{XC}}}{\partial \rho_{\uparrow}} + \frac{\partial f^{\text{XC}}}{\partial \rho_{\downarrow}} \right] \xi_{\mu}^{\vec{0}}(\vec{r}) \xi_{\nu}^{\vec{L}}(\vec{r}) d^3r \\ &\quad - \int \left[ 2 \frac{\partial f^{\text{XC}}}{\partial \gamma_{\uparrow\uparrow}} \vec{\nabla}\rho_{\uparrow} + 2 \frac{\partial f^{\text{XC}}}{\partial \gamma_{\downarrow\downarrow}} \vec{\nabla}\rho_{\downarrow} + \frac{\partial f^{\text{XC}}}{\partial \gamma_{\uparrow\downarrow}} (\vec{\nabla}\rho_{\uparrow} + \vec{\nabla}\rho_{\downarrow}) \right] \\ &\quad \left[ \left\{ \vec{\nabla}\xi_{\mu}^{\vec{0}}(\vec{r}) \right\} \xi_{\nu}^{\vec{L}}(\vec{r}) + \xi_{\mu}^{\vec{0}}(\vec{r}) \left\{ \vec{\nabla}\xi_{\nu}^{\vec{L}}(\vec{r}) \right\} \right] d^3r \\ &\quad + \int \frac{1}{2} \left[ \frac{\partial f^{\text{XC}}}{\partial \tau_{\uparrow}} + \frac{\partial f^{\text{XC}}}{\partial \tau_{\downarrow}} \right] \left[ \vec{\nabla}\xi_{\mu}^{\vec{0}}(\vec{r}) \right] \cdot \left[ \vec{\nabla}\xi_{\nu}^{\vec{L}}(\vec{r}) \right] d^3r \end{aligned} \quad (40)$$

for the scalar contribution, which is multiplied with  $\sigma_0$ , and

$$\begin{aligned} X_{\mu\nu,u}^{\vec{L}} &= \frac{\rho_{\text{m}}^u}{|\vec{\rho}_{\text{m}}|} \int \left[ \frac{\partial f^{\text{XC}}}{\partial \rho_{\uparrow}} - \frac{\partial f^{\text{XC}}}{\partial \rho_{\downarrow}} \right] \xi_{\mu}^{\vec{0}}(\vec{r}) \xi_{\nu}^{\vec{L}}(\vec{r}) d^3r \\ &\quad - \int \left[ 2 \frac{\partial f^{\text{XC}}}{\partial \gamma_{\uparrow\uparrow}} \vec{\nabla}\rho_{\uparrow} - 2 \frac{\partial f^{\text{XC}}}{\partial \gamma_{\downarrow\downarrow}} \vec{\nabla}\rho_{\downarrow} - \frac{\partial f^{\text{XC}}}{\partial \gamma_{\uparrow\downarrow}} (\vec{\nabla}\rho_{\uparrow} - \vec{\nabla}\rho_{\downarrow}) \right] \\ &\quad \left[ \left\{ \vec{\nabla}\xi_{\mu}^{\vec{0}}(\vec{r}) \right\} \xi_{\nu}^{\vec{L}}(\vec{r}) + \xi_{\mu}^{\vec{0}}(\vec{r}) \left\{ \vec{\nabla}\xi_{\nu}^{\vec{L}}(\vec{r}) \right\} \right] d^3r \\ &\quad + \int \frac{1}{2} \left[ \frac{\partial f^{\text{XC}}}{\partial \tau_{\uparrow}} - \frac{\partial f^{\text{XC}}}{\partial \tau_{\downarrow}} \right] \left[ \vec{\nabla}\xi_{\mu}^{\vec{0}}(\vec{r}) \right] \cdot \left[ \vec{\nabla}\xi_{\nu}^{\vec{L}}(\vec{r}) \right] d^3r \end{aligned} \quad (41)$$

for the spin contributions with  $u \in \{x, y, z\}$ . The four spin blocks for the Kohn-Sham-Fock equations, c.f. Eqs. (9)–(11), can be evaluated from Eqs. (40) and (41) according to

$$X_{\mu\nu}^{\alpha\alpha,\vec{L}} = \frac{1}{2}(X_{\mu\nu,0}^{\vec{L}} + X_{\mu\nu,z}^{\vec{L}}), \quad (42)$$

$$X_{\mu\nu}^{\beta\beta,\vec{L}} = \frac{1}{2}(X_{\mu\nu,0}^{\vec{L}} - X_{\mu\nu,z}^{\vec{L}}), \quad (43)$$

$$X_{\mu\nu}^{\alpha\beta,\vec{L}} = \frac{1}{2}(X_{\mu\nu,x}^{\vec{L}} - iX_{\mu\nu,y}^{\vec{L}}), \quad (44)$$

$$X_{\mu\nu}^{\beta\alpha,\vec{L}} = \frac{1}{2}(X_{\mu\nu,x}^{\vec{L}} - iX_{\mu\nu,y}^{\vec{L}})^*. \quad (45)$$

The evaluation of the exchange-correlation matrix blocks is based on numerical integration on a grid and the hierarchical scheme presented in Ref. [66]. Details on the underlying molecular 2c implementation can be found in Refs. [37–39].

This non-collinear formalism is needed for open-shell systems. For closed-shell systems, the real and symmetric part of the spin-vector density matrix vanishes due to Kramers' theorem, i.e.  $\text{Re}(D_{\nu\mu}^{\alpha\beta,\vec{L}}) + \text{Re}(D_{\nu\mu}^{\beta\alpha,\vec{L}})$ ,  $\text{Im}(D_{\nu\mu}^{\alpha\beta,\vec{L}}) - \text{Im}(D_{\nu\mu}^{\beta\alpha,\vec{L}})$ , and  $\text{Re}(D_{\nu\mu}^{\alpha\alpha,\vec{L}}) - \text{Re}(D_{\nu\mu}^{\beta\beta,\vec{L}})$  are zero. Further, time-reversal symmetry holds for closed-shell systems. Therefore, the general 2c formalism can be reduced to a Kramers-restricted (KR) framework and the XC potential can be evaluated as done in the 1c formalism. In contrast, the Kramers-unrestricted (KU) formalism without time-reversal symmetry is needed for open-shell systems.

## B. Two-Component Energy Gradients

Energy gradients are required to optimize coordinates of atoms in the unit cell and to optimize the corresponding lattice vectors based on the stress tensor [68, 75–79]. The derivative of the SCF energy with respect to a nuclear displacement reads

$$E_{\text{SCF}}^{I,\lambda} = E_{\text{T}}^{I,\lambda} + E_{\text{J}}^{I,\lambda} + E_{\text{SO}}^{I,\lambda} + E_{\text{XC}}^{I,\lambda} + E_{\text{NN}}^{I,\lambda}, \quad (46)$$

where the superscript  $\{I, \lambda\}$  indicates that we move the nucleus  $I$  in the reference cell  $\vec{L} = \vec{0}$  along the Cartesian direction  $\lambda$ . For the positions  $R_I^{\vec{L}} = R_I^{\vec{0}} + \vec{L}$  holds. Note that derivatives are generally formed in the limit of a vanishing perturbation [80, 81]. The nuclear repulsion term  $E_{\text{NN}}^{I,\lambda}$  associated with  $V_{\text{NN}}^{\vec{L}}$  is trivial and the same as in the non-relativistic limit and the 1c methodology. According to Pulay, none of the derivatives includes a response of the density matrix [82]. This finding holds for both DFT and Hartree–Fock theory based on converged 1c or 2c SCF procedures [83]. Instead of such an explicit response, the energy-weighted density matrix  $W$  arises for the first term given by

$$E_{\text{T}}^{I,\lambda} = \sum_{\mu\nu} \sum_{\vec{L}} \left( T_{\mu\nu}^{\vec{L}} \right)^{I,\lambda} \left[ \text{Re}(D_{\nu\mu}^{\alpha\alpha,\vec{L}}) + \text{Re}(D_{\nu\mu}^{\beta\beta,\vec{L}}) \right] - \sum_{\mu\nu} \sum_{\vec{L}} \left( S_{\mu\nu}^{\vec{L}} \right)^{I,\lambda} \left[ \text{Re}(W_{\nu\mu}^{\alpha\alpha,\vec{L}}) + \text{Re}(W_{\nu\mu}^{\beta\beta,\vec{L}}) \right]. \quad (47)$$

Here, the energy-weighted density matrix is defined as

$$W_{\nu\mu}^{\sigma\sigma',\vec{L}} = \frac{1}{V_{\text{FBZ}}} \sum_{i=1}^n \int_{\text{FBZ}}^{\epsilon_i^{\vec{k}} < \epsilon_{\text{F}}} e^{i\vec{k}\cdot\vec{L}} \left( c_{\nu i}^{\sigma,\vec{k}} \epsilon_i^{\vec{k}} c_{\mu i}^{*\sigma',\vec{k}} \right) d^3k, \quad (48)$$

which only differs from the density matrix by the inclusion of the spinor energy  $\epsilon_i$  in the integral, c.f. Eq. (18). Owing to the properties of the overlap matrix, we only need the real part of the diagonal spin blocks, i.e.  $\sigma = \sigma'$ , which is the analog of the particle density matrix. Therefore, this term can be implemented straightforwardly based on the 1c routines.

The derivative of the Coulomb energy  $E_{\text{J}}^{I,\lambda}$  does not depend on the spin density but only on the particle density. Therefore, its derivative is the same as in the 1c formalism. Thus, it consists of a crystal near field and a crystal far field contribution

$$E_{\text{J}}^{I,\lambda} = E_{\text{J,CNF}}^{I,\lambda} + E_{\text{J,CFF}}^{I,\lambda}. \quad (49)$$

They are defined in Ref. [68], and we point to this reference for details.

For the spin-orbit ECPs, the derivative  $E_{\text{SO}}^{I,\lambda}$  follows similarly to the kinetic energy contribution, and can be expressed as

$$E_{\text{SO}}^{I,\lambda} = \sum_{\vec{L}} \int \left[ \left( \vec{h}^{\text{SO},\vec{L}} \right)^{I,\lambda} \cdot \vec{\rho}_{\text{m}}^{\vec{L}}(\vec{r}, \vec{r}') \right]_{\vec{r}=\vec{r}'} d^3r. \quad (50)$$

Consequently the one-electron SOECP integral derivatives are simply contracted with the antisymmetric linear combinations of the complex AO density matrix. These are the same as for the SCF energy calculation, i.e.  $\text{Im}(D_{\nu\mu}^{\alpha\beta,\vec{L}}) + \text{Im}(D_{\nu\mu}^{\beta\alpha,\vec{L}})$ ,  $\text{Re}(D_{\nu\mu}^{\alpha\beta,\vec{L}}) - \text{Re}(D_{\nu\mu}^{\beta\alpha,\vec{L}})$ , and  $\text{Im}(D_{\nu\mu}^{\alpha\alpha,\vec{L}}) - \text{Im}(D_{\nu\mu}^{\beta\beta,\vec{L}})$ .

Finally, the derivative of the exchange-correlation energy  $E_{\text{XC}}^{I,\lambda}$  is needed. Again, no derivative of the density matrix arises for first-order derivatives. Therefore, we only need to form the derivative of the (non-collinear) XC potential matrix

$$\left( X_{\mu\nu}^{\vec{L}} \right)^{I,\lambda} = \left( \int \xi_{\mu}^{\vec{0}}(\vec{r}) \mathbf{V}^{\text{XC}}(\vec{r}) \xi_{\nu}^{\vec{L}}(\vec{r}) d^3r \right)^{I,\lambda}. \quad (51)$$

That is, the derivatives of  $X_{\mu\nu,0}^{\vec{L}}$  and  $X_{\mu\nu,u}^{\vec{L}}$  from Eqs. (40) and (41) (with  $u \in \{x, y, z\}$ ) are calculated and contracted directly with the respective density matrices to form  $E_{\text{XC}}^{I,\lambda}$ . These derivatives are now essentially given by the calculation of the gradient of a product of Gaussian basis functions and the existing functional ingredients for SCF energies, c.f. Refs. [84, 85]. Weight derivatives for the numerical integration of the XC part are included based on the 2c generalization of previous work in Refs. [66, 68, 75]. For closed-shell systems, the Kramers restriction and time-reversal symmetry can be exploited as done for SCF energies. This way, the 2c Kramers-restricted implementation is almost completely available from an existing 1c implementation.

## C. Stress Tensor

Unit cell parameters are optimized with the stress tensor [75, 78, 79] according to

$$\frac{\partial E_{\text{SCF}}}{\partial v_{n,p}} = \sum_{q=\{x,y,z\}} V_{\text{UC}} \sigma_{pq} (\mathbf{A}^{-1})_{nq} - \sum_{q=\{x,y,z\}} \sum_I \frac{\partial E_{\text{SCF}}}{\partial R_{I,p}} R_{I,q} (\mathbf{A}^{-1})_{nq} \quad (52)$$

where  $\mathbf{A}$  is a  $(3 \times 3)$  matrix consisting of the three vectors  $\vec{v}_n$  describing the unit cell of a three dimensional periodic system. The stress tensor components  $\sigma_{pq}$  are given by

$$\sigma_{pq} = \frac{1}{V_{\text{UC}}} \frac{\partial E_{\text{SCF}}}{\partial \epsilon_{pq}} \quad (53)$$

with the volume of the unit cell  $V_{\text{UC}}$  and the symmetric strain tensor  $\epsilon_{pq}$ . The latter describes the transformation of an atomic position  $\vec{R}_I$  in a direct lattice cell  $\vec{L}$  with respect to an elastic deformation, i.e.

$$\left( R_{I,p}^{\vec{L}} \right)' = \sum_{q=\{x,y,z\}} (\delta_{pq} + \epsilon_{pq}) R_{I,q}^{\vec{L}} \quad (54)$$

with the Cartesian components  $p, q \in \{x, y, z\}$  and the Kronecker delta  $\delta_{pq}$ . The stress tensor follows as a sum over UC contributions

$$\sigma_{pq} = \frac{1}{V_{\text{UC}}} \sum_{\vec{L}} \sum_N \frac{\partial E_{\text{SCF}}}{\partial R_{N,p}^{\vec{L}}} R_{N,q}^{\vec{L}} \quad (55)$$

and the derivatives are obtained using Eq. (46). This leads to

$$\begin{aligned} \sigma_{pq} = & \frac{1}{V_{\text{UC}}} \sum_{\vec{L}} \sum_I \left[ \frac{\partial E_{\text{T}}}{\partial R_{I,p}^{\vec{L}}} + \frac{\partial E_{\text{J}}}{\partial R_{I,p}^{\vec{L}}} + \frac{\partial E_{\text{NN}}}{\partial R_{I,p}^{\vec{L}}} \right] R_{I,q}^{\vec{L}} \\ & + \frac{1}{V_{\text{UC}}} \sum_{\vec{L}} \sum_I \left[ \frac{\partial E_{\text{SO}}}{\partial R_{I,p}^{\vec{L}}} + \frac{\partial E_{\text{XC}}}{\partial R_{I,p}^{\vec{L}}} \right] R_{I,q}^{\vec{L}}, \end{aligned} \quad (56)$$

where the kinetic energy term again includes the energy-weighted density matrix

$$\begin{aligned} \frac{\partial E_{\text{T}}}{\partial R_{N,p}^{\vec{L}}} = & \sum_{\mu\nu} \sum_{\vec{L}'} \frac{\partial T_{\mu\nu}^{\vec{L}'}}{\partial R_{N,p}^{\vec{L}}} \left[ \text{Re}(D_{\nu\mu}^{\alpha\alpha, \vec{L}'}) + \text{Re}(D_{\nu\mu}^{\beta\beta, \vec{L}'}) \right] \\ & - \sum_{\mu\nu} \sum_{\vec{L}'} \frac{\partial S_{\mu\nu}^{\vec{L}'}}{\partial R_{N,p}^{\vec{L}}} \left[ \text{Re}(W_{\nu\mu}^{\alpha\alpha, \vec{L}'}) + \text{Re}(W_{\nu\mu}^{\beta\beta, \vec{L}'}) \right]. \end{aligned} \quad (57)$$

Hence, the calculation of the stress tensor contributions essentially reduces to the calculation of derivatives with respect to nuclear displacements. The Coulomb contribution is evaluated like in the non-relativistic or scalar 1c limit [75], whereas the calculation of the SOECP and XC terms in Eq. (56) requires more AO density matrix linear combinations. The derivatives of  $E_{\text{SO}}$  use the antisymmetric linear combinations  $\text{Im}(D_{\nu\mu}^{\alpha\beta, \vec{L}'}) + \text{Im}(D_{\nu\mu}^{\beta\alpha, \vec{L}'})$ ,  $\text{Re}(D_{\nu\mu}^{\alpha\beta, \vec{L}'}) - \text{Re}(D_{\nu\mu}^{\beta\alpha, \vec{L}'})$ , and  $\text{Im}(D_{\nu\mu}^{\alpha\alpha, \vec{L}'}) - \text{Im}(D_{\nu\mu}^{\beta\beta, \vec{L}'})$  for the contraction with  $\partial h_{\mu\nu}^{j, \vec{L}'}/\partial R_{N,p}^{\vec{L}}$ , with  $j$  denoting the spin-orbit components  $x, y, z$ . For the XC contribution, the respective derivatives of  $X_{\mu\nu,0}^{\vec{L}'}$  and  $X_{\mu\nu,u}^{\vec{L}'}$  are contracted with the symmetric AO density matrices  $\text{Re}(D_{\nu\mu}^{\alpha\alpha, \vec{L}'}) + \text{Re}(D_{\nu\mu}^{\beta\beta, \vec{L}'})$  for the scalar contributions, and  $\text{Re}(D_{\nu\mu}^{\alpha\beta, \vec{L}'}) + \text{Re}(D_{\nu\mu}^{\beta\alpha, \vec{L}'})$ ,  $\text{Im}(D_{\nu\mu}^{\alpha\beta, \vec{L}'}) - \text{Im}(D_{\nu\mu}^{\beta\alpha, \vec{L}'})$ ,

and  $\text{Re}(D_{\nu\mu}^{\alpha\alpha, \vec{L}'}) - \text{Re}(D_{\nu\mu}^{\beta\beta, \vec{L}'})$  for the non-collinear  $x, y$ , and  $z$  components. The evaluation of the derivatives of the XC potential ingredients ( $\partial f^{\text{XC}}/\partial \rho, \xi_\mu$ , etc.) is done as described in Refs. [74, 75, 86, 87]. We emphasize that weight derivatives of the DFT part are of great importance for the stress tensor [86, 88] and consequently always included based on Refs. [74, 87].

## D. Implementation

Due to the integral evaluation in real space, our implementation is largely based on the existing molecular implementations [37–39]. That is, the SOECP integrals are evaluated with the McMurchie–Davidson scheme [89, 90]. All one- and two-electron integral routines are parallelized with the OpenMP paradigm [91, 92]. Algebraic operations make use of the Math Kernel Library (MKL). Depending on the size of the basis set and the number of  $k$  points in reciprocal space, parallelization is either done over the  $k$  points or for the algebraic operations and transformations inside the loop over  $k$  points. The first option is used with many  $k$  points and comparably small basis sets, whereas the second option is used for large basis sets with more than, e.g., 5,000 functions in the sparse Cartesian AO basis. The direct inversion in the iterative subspace (DIIS) is exploited to accelerate the SCF convergence [93] in its  $\Gamma$  point version. Interfaces to LIBXC [94–96] are provided to support (almost) all semilocal density functional approximations.

Our implementation supports the SCF initial construction of the band structure based on a molecular Hückel guess, converged 1c molecular orbitals (MOs), 2c molecular spinors, or 1c bands. The Kramers-restricted framework can only be used on top of MOs or bands of an RKS calculation. For the KU formalisms, the starting wave function can be constructed as an eigenfunction of the spin functions  $S_x, S_y$ , or  $S_z$ . For simplicity, we use the last option as default setting.

The 2c geometry gradients and the related stress tensor were also implemented based on the 1c routines [68, 75]. The SOECP integral derivatives are currently evaluated numerically, c.f. the molecular implementation in Ref. [38]. The other contributions use analytical integral derivatives. All integral derivatives are parallelized with the OpenMP scheme. Structures can be optimized with Grimme’s DFT dispersion correction D3 including zero or Becke–Johnson damping [72, 73], if desired.

## E. SCF Calculation Times

Tab. I shows the computation time per iteration step in seconds for a three-dimensional face-centered cubic (fcc) Pb crystal (primitive unit cell vectors length 3.500 Å), employing 1c restricted Kohn–Sham (RKS), 1c unrestricted Kohn–Sham (UKS), 2c GKS KR, and 2c GKS KU frameworks. Here, we used the singlet state as initial guess, since this is the ground state in 2c calculations.

TABLE I. Computation time in seconds for the SCF steps and number of iterations for a calculation of a three-dimensional Pb crystal (PBE functional [97], dhf-TZVP-2c basis [98]) with a single thread of an Intel Xeon Gold 6212U central processing unit @ 2.40 GHz. The number of atoms per unit cell is one, the number of  $k$  points is 32,768 and the chosen grid size for the exchange-correlation potential is 4 (very large) [99, 100]. The code was compiled with Intel Fortran Compiler 19.0.1.144 without setting just-in-time flags. Bands are stored in binary format, while the MOs or spinors of the unit cell are stored in ASCII format (Band/MO dump). The SCF initial guess is obtained by constructing bands from Hückel theory.  $D_{\mu\nu}$  Build refers to the construction of the density matrices in real space,  $J$  to the evaluation of the Coulomb integrals, and XC to the numerical integration of the XC potential. Diag and Iter denote the diagonalization for the Kohn–Sham equations and the number of iterations. Note that the energy contributions from the Coulomb term  $J$  and the XC part are again calculated after the last iteration. Timings for the overlap and kinetic energy matrix are omitted, as they are negligible.

	Pre-SCF		SCF					Post-SCF		Total
	ECP	SOECP	$D_{\mu\nu}$ Build	$J$	XC	Diag	Time	Iter	Dump	
1c RKS	4.7	–	12.3	33.8	38.4	20.1	108.8	14	53.0	1656.4
1c UKS	4.9	–	24.7	33.8	50.6	39.6	156.7	14	104.6	2488.2
2c GKS KR	4.7	38.0	49.4	33.5	37.9	82.7	214.3	14	150.2	3253.5
2c GKS KU	4.9	38.4	96.9	33.6	90.4	231.3	483.9	14	301.7	7050.8

The number of atoms per unit cell is one, the number of  $k$  points used is 32,768 and the chosen grid size for the exchange-correlation potential is 4 (“ultrafine”) [99, 100]. Note that all frameworks except for 2c GKS KU use time-reversal symmetry for the  $k$  points. The PBE functional [97] was combined with the dhf-TZVP-2c orbital and auxiliary basis set [98]. Thus, small-core Dirac–Fock ECPs are applied (ECP-60) [101]. SCF thresholds of  $10^{-8}$  Hartree for the energy are chosen. Gaussian smearing is used with a criterion of 0.005 Hartree. For comparison, the initial bands are obtained from a standard Hückel guess.

The extension from a 1c to a 2c formalism has a crucial impact on the running time of the SCF procedure, due to the complex nature of the SCF orbitals in real space. This covers the following major steps.

- **Construction of the density matrix.** For the 2c KU formalism, the particle density  $\rho_p$  and the spin densities  $\rho_m^x$ ,  $\rho_m^y$ , and  $\rho_m^z$  have to be constructed for both the  $+\vec{k}$  and  $-\vec{k}$  points. Additionally, the densities for the contraction with the SOECP part are needed. Formally, this leads to a factor of eight, however, several densities can be processed simultaneously and symmetric/antisymmetric linear combinations are formed. In the KR framework, time-reversal symmetry is used as done for the 1c approaches. Thus, only half the number of  $k$  points is needed and the computation time is reduced accordingly.
- **Coulomb matrix.** There is no structural change for the Coulomb part and no increase of the computation time.
- **Exchange-correlation matrix.** Analogous to the density matrix, within the 2c KU formalism it is necessary to evaluate four densities  $\rho_p$ ,  $\rho_m^x$ ,  $\rho_m^y$ , and  $\rho_m^z$  on the numerical lattice. Compared to the 1c RKS procedure, this leads to a factor of four, or a factor of two compared to the 1c UKS procedure. The 2c KR approach does not lead to any extra costs relative to the 1c RKS ansatz.

- **Diagonalization of the Kohn–Sham–Fock matrix.** For periodic systems, a single diagonalization of the Kohn–Sham–Fock matrix is eight times more involved compared to a 1c RKS calculation, as the dimensionality of matrices doubles due to 2c construction. Hence the computation time of a diagonalization scales like  $N_{\text{BF}}^3$ . In UKS theory, the spin components of the Kohn–Sham–Fock matrix can be decoupled, which is not possible in 2c GKS due to spin–orbit interaction.

The time investment needed for the diagonalization of the Kohn–Sham–Fock matrix depends on two factors, i.e. on the number of basis functions  $N_{\text{BF}}$  and the total number of  $k$  points  $N_k$ , as one diagonalization per  $k$  point is executed. This means that the computational costs of the diagonalization are proportional to  $N_{\text{BF}}^3$  and to  $N_k$ . For smaller systems in terms of basis functions, the diagonalization time plays only a minor role for the total computation time. Ultimately, it is obvious that the diagonalization time for the 2c calculations is substantially larger than for the 1c calculations.

We conclude that for periodic systems, the 2c formalism provides an efficient way of dealing with physics based on spin–orbit coupling. To reduce the computational costs, the unit cell size can be decreased to the minimally necessary extent, while simultaneously increasing the number of  $k$  points in order to retain the same effective system size. This way, a linear increase of the computational demands proportional to  $N_k$  rather than the cubic proportionality of  $N_{\text{BF}}^3$  can be exploited. That allows us to perform calculations on large systems in a reasonable amount of time with low-cost computer hardware. Note, that this statement is not only true for 2c periodic calculations but for periodic calculations in general.

### III. APPLICATION TO PERIODIC SYSTEMS OF ARBITRARY DIMENSION

In this section, we present calculations of various systems to illustrate applications of the 2c GTO-based approach and to show differences of the electronic structure by the inclusion of spin-orbit coupling. Computational details are discussed in each subsection.

#### A. Ionization Energies of Heavy $p$ -Block Atoms: Zero-Dimensional Systems

To begin with, we validate the implementation by comparison to the existing 2c molecular version. Therefore, we study the ionization energy of heavy  $p$  elements, referring to the 2c implementation for atoms, molecules, and clusters in the RIDFT module [37, 38, 102–104]. Compared to lighter elements, the ionization energies of heavy  $5p$  and  $6p$  elements follow a different trend. While the light elements feature an increasing ionization energy from left to right in the periodic table with especially stable half-filled sub-shells [105, 106], this is not the case for the heavy elements as they feature a heavier core and, therefore, stronger spin-orbit coupling. Strong spin-orbit coupling is accompanied by a larger splitting of  $p$ ,  $d$ , and  $f$  orbitals. Here, the splitting of the  $p$  shell is of particular importance. The  $p$  shells split into two-fold degenerated  $p_{1/2}$  and four-fold degenerated  $p_{3/2}$  orbitals, indicating a stable  $p^2$  configuration for lead. Thus, the ground state of lead is a triplet based on 1c calculations, while it is a singlet in 2c approaches.

According to the results in Tab. II, the computed ionization energies validate this trend. For all calculations, the dhf-SVP-2c GTO basis set [98] with small-core Dirac-Fock ECPs [101] and the PBE exchange-correlation functional [97] were employed (grid size 4 [99, 100], “ultra-fine”). The 2c procedure shows a good qualitative agree-

TABLE II. Ionization energies (absolute value of the highest occupied orbital or spinor state) for the heavy  $p$ -block elements In–I and Tl–At. To ensure comparability for all calculations, the dhf-SVP-2c Gaussian basis set [98] with small-core Dirac-Fock ECPs [101] and the PBE exchange-correlation functional [97] were employed. The experimentally determined ionization potentials (Experiment) can be found in Ref. [107]. All values are given in eV.

	In	Se	Sb	Te	I
1c RIPER	5.58	7.26	8.95	9.42	10.42
2c RIPER	5.70	7.14	8.67	8.86	10.31
2c RIDFT	5.70	7.14	8.67	8.86	10.31
Experiment	5.70	7.34	8.64	9.01	10.45
	Tl	Pb	Bi	Po	At
1c RIPER	5.41	6.97	8.55	8.98	9.99
2c RIPER	6.06	7.12	7.26	8.32	9.16
2c RIDFT	6.06	7.12	7.26	8.32	9.16
Experiment	6.11	7.42	7.29	8.43	9.54

ment with the experimental values, while the 1c calculations exhibit partly large deviations. On quantitative considerations, the 2c simulations yield an average deviation of 0.12 eV from the experimental values, while we find an average deviation of 0.46 eV for the 1c procedure. Calculations with the RIDFT module lead to the same values as the RIPER module, demonstrating consistency.

#### B. Band Structures of Three-Dimensional Gold and Lead Crystals

Next, we demonstrate the consistency of our implementation with well-established codes such as the plane-wave QUANTUM ESPRESSO program [108]. We thus study the band structures of three-dimensional gold and lead crystals. Figure 1 shows the simulated electronic band structure for bulk gold and lead, forming an optimal fcc lattice with a lattice constant of  $a = 4.0800 \text{ \AA}$  and  $a = 4.9508 \text{ \AA}$ , respectively [109].

For the RIPER calculations (1c, 2c), the dhf-TZVP-2c GTO basis set [98] with small-core Dirac-Fock ECPs [101, 110] (ECP-60 for Au and Pb) and the PBE functional [97] were employed (grid size 4). A  $k$  point mesh of  $32 \times 32 \times 32$  is used in combination with a Gaussian smearing of 0.005 Hartree [111] to ensure convergence. Total SCF energies are converged up to  $10^{-8}$  Hartree. For the QUANTUM ESPRESSO calculations, we used the relativistic pseudopotentials `Au.rel-pbe-dn-rrkjus-ps1.0.1.UPF` for gold and `Pb.rel-pbe-dn-rrkjus-ps1.0.2.2.UPF` for lead, respectively. Cutoff radii of 200 Ry for the wave functions and 2000 Ry for the electron density were set, while the other parameters such as the number of  $k$  points, the Gaussian smearing, and the convergence threshold are the same as for the RIPER calculations to ensure comparability.

The impact of spin-orbit interactions on the band structure of gold can be quantified by comparing purple and orange curves in Fig. 1a. We find that the influence of spin-orbit interactions is of minor relevance for bulk gold. For large parts of the electronic band structures, both curves are in excellent agreement, especially close to the Fermi level at  $\epsilon_F = 0 \text{ eV}$ . The most prominent deviations between 1c and 2c calculations are the splitting of the band crossing point at about 5.5 eV for the W point and at around  $-5 \text{ eV}$  for the  $\Gamma$  point. The comparison of the band structure of the 2c RIPER (purple) and the QUANTUM ESPRESSO (red) calculations reveals a good agreement of energies below and around the Fermi level  $\epsilon_F = 0 \text{ eV}$ . This indicates consistent results of the 2c RIPER implementation and the plane-wave QUANTUM ESPRESSO code, while providing the reduced calculation times of GTO over plane-wave basis sets. However, the band structures exhibit larger deviations in the region above 7 eV. This is not surprising as plane-wave basis sets are known to be superior in the description of the energy states in the continuum above the gold work function, which amounts to around 5 eV [112].



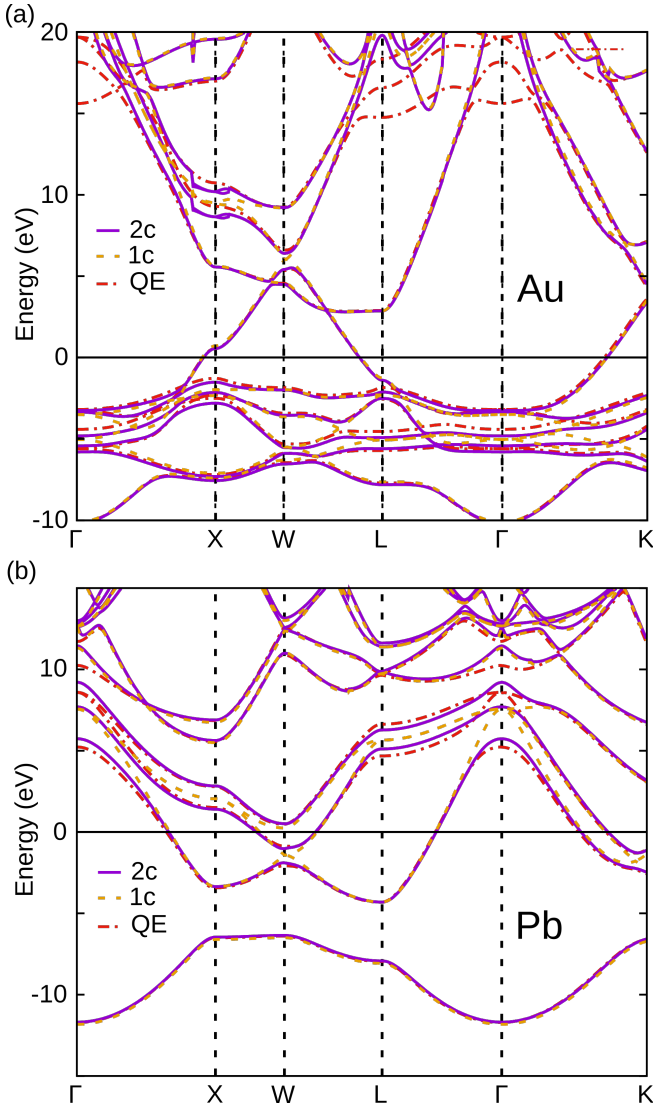


FIG. 1. Simulated band structure for (a) an fcc bulk gold crystal (lattice constant  $a = 4.0800 \text{ \AA}$  [109]) and (b) an fcc bulk lead crystal ( $a = 4.9508 \text{ \AA}$  [109]). Results for the RIPER module with (2c) and without (1c) spin-orbit coupling are shown together with relativistic calculations using the QUANTUM ESPRESSO (QE) code [108]. All computations employ the PBE functional [97]. We use the dhf-TZVP-2c GTO basis set for RIPER and a plane-wave basis for QUANTUM ESPRESSO. Vertical dashed lines mark high symmetry points of the FBZ.

In contrast to gold, the band structures of lead in Fig. 1b reveal a more pronounced impact of spin-orbit coupling due to the heavier atoms. Comparison of the 1c (orange) and the 2c (purple) RIPER band structures shows a band splitting of  $0.87 \text{ eV}$  at the W point for  $-1.5 \text{ eV}$ . That is, the proper description of bulk electronic structures of heavy  $p$  block systems generally necessitates the consideration of spin-orbit interactions. Figure 1b furthermore shows a similar behavior concerning the quality of our implementation for bulk lead. For energies below and around the Fermi level  $\epsilon_F = 0 \text{ eV}$ , the band structures of both the relativistic QUANTUM

ESPRESSO (red) and the 2c RIPER (purple) calculations match almost perfectly. In contrast, deviations are observed for energies above ca.  $5 \text{ eV}$ . Again, this is a consequence of the better description of high energy states close to the continuum with plane-wave basis sets, the work function of Pb amounting to around  $4 \text{ eV}$  [113].

### C. Band Gaps of Three-Dimensional Silver Halide Crystals

Silver halide crystals  $\text{AgX}$  ( $X = \text{Cl}, \text{Br}, \text{I}$ ) are typical model systems to study relativistic effects [114–117]. Studies have been performed with relativistic all-electron and ECP-based or quasi-relativistic Hamiltonians. Due to the small gaps and the densely packaged crystal structures, the systems are a challenging case for computational simulations [116]. In Tab. III, we compare results with the ECP-based implementation to previously reported ones from relativistic all-electron approaches including all-electron exact two-component (X2C) theory [115] and the four-component (4c) Dirac–Kohn–Sham (DKS) ansatz directly based on the many-electron Dirac–Coulomb equation [116].

Computational methods are chosen in accordance with previous studies [114–116]. Lattice constants are taken from Ref. [114], i.e.  $a = 5.612 \text{ \AA}$  for AgCl,  $a = 5.843 \text{ \AA}$  for AgBr, and  $a = 6.169 \text{ \AA}$  for AgI. Calculations are carried out with the primitive unit cell and a  $k$  mesh of  $7 \times 7 \times 7$  points. Increasing this to  $12 \times 12 \times 12$  changed the energy of AgCl by less than  $3 \cdot 10^{-6}$  Hartree. SCF convergence thresholds are set to  $10^{-7}$  Hartree. Non-relativistic calculations are performed with the def2-TZVP [118] (Cl, Br), TZVPalls2 (Ag), and the TZVPall (I) all-electron basis sets [119]. Scalar-relativistic and spin-orbit calculations employ the dhf-SVP basis sets [98] together with small-core Dirac–Fock ECPs (ECP-28) [120, 121]. Note that we always transform the Kohn–Sham–Fock matrices into an orthogonal basis by diagonalization of the overlap matrix (threshold  $10^{-6}$ ) [67]. Thus, we have not removed diffuse functions (exponents smaller than  $0.1 \text{ Bohr}^{-1}$ ).

We find that the non-relativistic framework is clearly insufficient for all systems, as it leads to a large deviation from the formally superior 4c DKS approach. Relativistic effects are mainly captured by scalar ECPs, i.e. the spatial and energetic contraction of the electron density is the leading relativistic correction. However, some band gaps such as the  $\Gamma$ – $\Gamma$  and the X–X gap of AgI require the inclusion of spin-orbit coupling, as it lowers the gap by  $0.2 \text{ eV}$ . Likewise, the  $\Gamma$ – $\Gamma$  and X–X gaps of AgCl and AgBr are notably affected.

The 2c-ECP approach leads to a good agreement with relativistic all-electron schemes. The qualitative trends of the band gaps are well described, and the 2c approach generally reduces the deviation towards the 4c DKS results. Exceptions in this regard are the X–X gaps of AgCl and AgBr. The same holds for scalar-relativistic and spin-orbit X2C calculations of the X–X gap of AgCl, see Refs. [115, 116]. For both ECPs and X2C, spin-orbit

TABLE III. Energy band gaps (in eV) of three-dimensional AgCl, AgBr, and AgI crystals (lattice constants  $a = 5.612 \text{ \AA}$ ,  $a = 5.843 \text{ \AA}$ ,  $a = 6.169 \text{ \AA}$ , all rocksalt structure) for high symmetry points of the FBZ with the PBE functional [97] and grid size 4. Non-relativistic calculations (NR) were performed with the def2-TZVP [118] (Cl, Br), TZVPalls2 (Ag) [119], and the TZVPall (I) basis sets [119], whereas the ECP-based 1c and 2c calculations use the dhf-SVP bases [98] and small-core Dirac-Fock ECPs [120, 121]. Results with scalar relativistic (SR) and spin-orbit (SO) X2C employing (truncated) Slater-type bases are taken from Ref. [115]. Four-component DKS results are taken from Ref. [116], employing uncontracted double- $\zeta$  basis sets [122–124].

AgCl	L-L	$\Gamma$ - $\Gamma$	X-X	L- $\Gamma$
NR	4.86	3.72	5.32	1.66
1c ECP	4.62	3.11	4.16	0.91
2c ECP	4.57	2.94	3.99	0.86
SR X2C	4.31	3.09	4.23	0.92
SO X2C	4.27	2.99	4.03	0.88
4c DKS	4.47	2.93	4.20	0.87
AgBr	L-L	$\Gamma$ - $\Gamma$	X-X	L- $\Gamma$
NR	4.28	3.19	4.77	1.56
1c ECP	4.07	2.64	3.70	0.86
2c ECP	3.91	2.62	3.48	0.77
SR X2C	3.87	2.43	3.87	0.68
SO X2C	3.77	2.25	3.67	0.60
4c DKS	3.82	2.24	3.68	0.61
AgI	L-L	$\Gamma$ - $\Gamma$	X-X	L-X
NR	3.89	3.42	3.71	1.48
1c ECP	3.49	2.16	2.98	0.65
2c ECP	3.25	1.82	2.69	0.64
SR X2C	3.42	2.27	3.07	0.74
SO X2C	3.17	1.90	2.76	0.49
4c DKS	3.25	1.88	2.74	0.49

effects lower these band gaps by about 0.2 eV. Hence, considering these effects worsens the respective results, which hints at subtle error cancellation.

For comparison, we study the impact of the basis set and the density functional approximation. For the DFT study, we consider the first three rungs of Jacob’s ladder. The local spin density approximation (LSDA) is represented by the S-VWN (III) functional [133, 134], whereas PBE [97] and PBEsol [135] serve as examples for generalized gradient approximations (GGAs). mGGAs are included with the TPSS [136], revTPSS [137, 138], Tao-Mo [139], PKZB [140], and r<sup>2</sup>SCAN [141, 142] approximations. Note that we use LIBXC [94–96] for the PBEsol, revTPSS, Tao-Mo, PKZB, and r<sup>2</sup>SCAN functionals. The dhf-SVP and dhf-TZVP basis sets were employed with fixed crystal structures, and results are listed in the Supplemental Material. In addition, cell structure optimizations with these exchange-correlation functionals were carried out with the dhf-SVP basis [98, 143], including the D3 correction with Becke-Johnson (BJ) damping if available [55, 72, 73, 144, 145]. All other computational parameters such as SCF thresholds and grids

TABLE IV. Optimized lattice constants  $a$  (in  $\text{\AA}$ , rocksalt structure) of three-dimensional AgCl, AgBr, and AgI crystals and energy band gaps (in eV) for high symmetry points of the FBZ with various density functional approximations and the dhf-SVP basis sets [98]. Experimental data taken from Refs. [125–132], as collected in Ref. [115].

AgCl		$a$	L-L	$\Gamma$ - $\Gamma$	X-X	L- $\Gamma$
S-VWN (III)	no D3	5.377	3.93	3.27	3.85	0.55
PBE	no D3	5.624	4.58	2.91	3.99	0.86
PBEsol	no D3	5.515	4.20	2.98	3.89	0.66
TPSS	no D3	5.586	4.55	3.04	4.13	0.97
revTPSS	no D3	5.561	4.38	3.02	4.13	0.89
Tao-Mo	no D3	5.541	4.24	3.10	4.24	0.97
PKZB	no D3	5.636	4.59	3.10	4.26	1.18
r <sup>2</sup> SCAN	no D3	5.576	5.02	3.55	4.56	1.41
PBE	D3 BJ	5.537	4.47	3.08	4.03	0.85
PBEsol	D3 BJ	5.426	4.07	3.20	3.93	0.66
TPSS	D3 BJ	5.498	4.40	3.21	4.18	0.94
revTPSS	D3 BJ	5.476	4.23	3.20	4.17	0.87
Tao-Mo	D3 BJ	5.511	4.20	3.17	4.25	0.97
r <sup>2</sup> SCAN	D3 BJ	5.517	4.94	3.68	4.59	1.42
Experiment		5.550		5.2		3.0
AgBr		$a$	L-L	$\Gamma$ - $\Gamma$	X-X	L- $\Gamma$
S-VWN (III)	no D3	5.604	3.42	2.82	3.39	0.54
PBE	no D3	5.849	4.03	2.63	3.54	0.82
PBEsol	no D3	5.692	3.60	2.77	3.45	0.65
TPSS	no D3	5.812	3.99	2.90	3.68	0.95
revTPSS	no D3	5.784	3.87	2.96	3.67	0.94
Tao-Mo	no D3	5.738	3.78	3.14	3.79	1.08
PKZB	no D3	5.868	4.13	2.99	3.81	1.19
r <sup>2</sup> SCAN	no D3	5.811	4.50	3.36	4.09	1.42
PBE	D3 BJ	5.747	3.89	2.82	3.57	0.83
PBEsol	D3 BJ	5.613	3.48	2.95	3.48	0.67
TPSS	D3 BJ	5.708	3.82	3.09	3.71	0.95
revTPSS	D3 BJ	5.690	3.72	3.14	3.70	0.94
Tao-Mo	D3 BJ	5.743	3.79	3.13	3.79	1.08
r <sup>2</sup> SCAN	D3 BJ	5.772	4.45	3.44	4.10	1.42
Experiment		5.774		4.3		2.5
AgI		$a$	L-L	$\Gamma$ - $\Gamma$	X-X	L-X
S-VWN (III)	no D3	5.937	2.73	1.96	2.70	0.46
PBE	no D3	6.187	3.27	1.79	2.67	0.64
PBEsol	no D3	6.023	2.88	1.93	2.74	0.54
TPSS	no D3	6.153	3.25	2.05	2.94	0.83
revTPSS	no D3	6.116	3.15	2.13	3.00	0.85
Tao-Mo	no D3	6.071	3.10	2.34	3.11	1.04
PKZB	no D3	6.200	3.41	2.15	2.99	1.02
r <sup>2</sup> SCAN	no D3	6.159	3.78	2.50	3.24	1.29
PBE	D3 BJ	6.067	3.11	1.99	2.78	0.69
PBEsol	D3 BJ	5.927	2.74	2.12	2.84	0.61
TPSS	D3 BJ	5.982	2.99	2.35	3.10	0.91
revTPSS	D3 BJ	5.949	2.88	2.44	3.16	0.94
Tao-Mo	D3 BJ	6.068	3.10	2.35	3.11	1.04
r <sup>2</sup> SCAN	D3 BJ	6.156	3.77	2.51	3.24	1.29
Experiment		6.067				

are unchanged, compared to the Hamiltonian study in Tab. III. The main results are listed in Tab. IV, see Supplemental Material for all results.

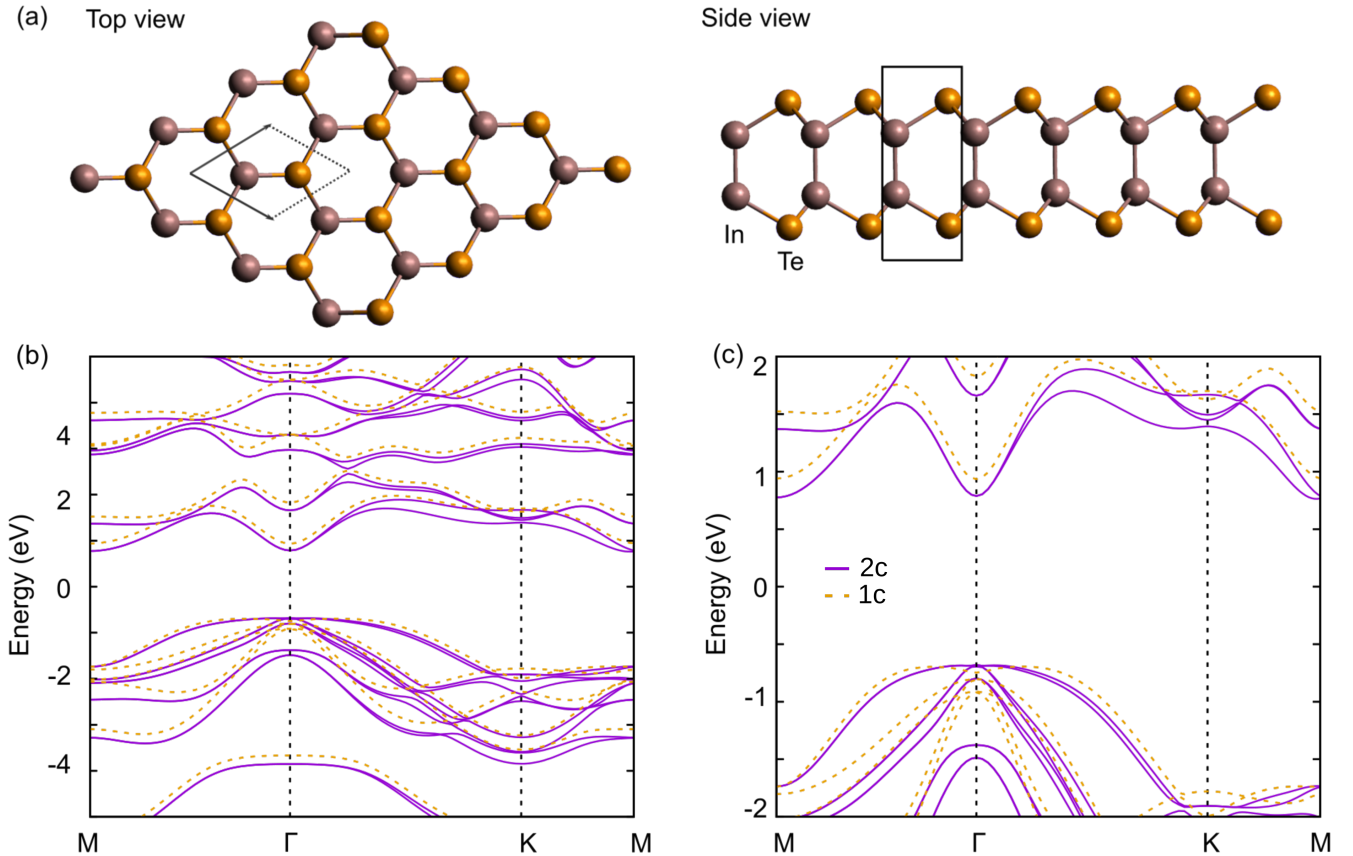


FIG. 2. (a) Top and side views of the two-dimensional InTe honeycomb system with indicated unit cell. The unit cell consists of two In and two Te atoms, marked with vertical black lines. (b, c) Electronic band structure of the FBZ. The orange dashed lines are calculated without spin-orbit coupling, while the solid purple lines include spin-orbit interactions. The black vertical dashed lines mark the  $\Gamma$  and K points of the Brillouin zone. Calculations are performed with the PBE functional [97], the D3-BJ dispersion correction [72, 73], and the dhf-TZVP-2c basis sets [98].

Obviously, the impact of the density functional approximations is much larger than the deviations between the 2c ECP and the all-electron X2C or DKS ansatz. Especially for the small  $L-\Gamma$  and  $L-X$  band gaps, the choice of the semilocal functional substantially affects the results. Here, the gaps increase from LSDA to GGA functionals and tend to further rise for the mGGAs. This finding also holds for the other band gaps of all AgX systems.

Dispersion correction leads to notably decreased lattice constants and thus indirectly affects the band gaps. For the lattice constants, the PBE-D3 functional performs best for AgCl, whereas  $r^2$ SCAN-D3 and Tao-Mo-D3 perform best for AgBr and AgI, respectively. According to the Supplemental Material, the larger tripe- $\zeta$  basis sets consistently lower the gaps, which is in agreement with similar studies at the DKS level in Ref. [116].

In conclusion, an ECP-based implementation is sufficient for the band gaps of silver halide crystals, as this property is driven by the valence region. In contrast, all-electron approaches may be needed for other properties which depend on the density close to the nuclei, or for a fully parameter-free approach to relativistic effects.

#### D. Indium(I,III)-Telluride Two-Dimensional Honeycomb System

To illustrate the applicability of the implementation to two-dimensional systems, we consider the indium(I,III)-telluride (InTe) honeycomb crystal displayed in Fig. 2a. For layered two-dimensional materials and their atomically thin layers dispersion interactions may play an important role. Here, we use the PBE functional [97] (grid size 4) combined with the D3 correction [72] and Becke-Johnson damping [73]. The dhf-TZVP-2c basis set [98] is applied, and a  $k$  mesh of  $32 \times 32$  is employed. A Gaussian smearing of 0.001 Hartree [111] and an SCF threshold of  $10^{-8}$  Hartree are chosen. The cell structure is optimized with the 2c Hamiltonian, and band structures are shown in Fig. 2b and 2c. For comparison, the electronic band structure based on the unit cell structure optimized without the D3-BJ correction and spin-orbit interaction is displayed in the Supplemental Material.

We find that the dispersion correction is important for the unit cell structure and the band gap. Without D3-BJ, a lattice constant of 4.17 Å, and band gaps of 1.56 eV

(1c) and 1.12 eV (2c) are obtained. Adding the D3-BJ correction changes the lattice constant to 4.23 Å. Band gaps are increased to 1.63 eV (1c) and 1.44 eV (2c). Thus, spin-orbit coupling changes the band gap by about 12% for the latter structure. To compare with, the impact of the D3-BJ correction on the unit cell structure is somewhat larger. Especially, the 2c band gap is substantially affected and sensitive to the unit cell structure. This reveals a delicate interplay of spin-orbit coupling and the cell structure.

The most notable changes of the electronic band structure induced by spin-orbit coupling are found for the  $\Gamma$  point in the energetic region from 1 to 2 eV below the Fermi level of  $\epsilon_F = 0$  eV. Here, the energies of the occupied bands are substantially decreased. The shifts for the two bands at about  $-1.5$  eV amount to more than 0.5 eV. Yet, the reduction of the bands gap from 1.63 to 1.44 eV due to spin-orbit coupling is mainly caused by the energetic decrease of the valence bands. Overall, our results are in rather good agreement with those of Shang *et al.* [146], who reported a band gap of 1.27 eV.

### E. One-Dimensional Platinum Chains

Transport through atomically thin wires serves as a sensitive probe of their electronic structure. Scalar-relativistic effects have been pointed out to be crucial for the chain formation in metallic atomic contacts of Ir, Pt, and Au [148]. From these three elements, Pt and Ir have been suggested to show interesting magnetic effects based on the spin-orbit coupling, such as an anisotropic magnetoresistance [20]. As chains are pulled, they transition from a zigzag to a linear configuration [149]. While linear chains are thus not the ground-state geometry for all interatomic distances, linear chains of Pt are by now a reference system for a transition to a magnetic state [20, 150–153]. We will reexamine this system with our new implementation here.

For the calculations, the PBE exchange-correlation functional [97] (grid size 4 [99, 100]), and the dhf-TZVP-2c GTO basis set [98] with small-core Dirac-Fock ECPs [110]. 32  $k$  points are used in combination with a Gaussian smearing of 0.01 Hartree [111]. SCF procedures were converged with a threshold of  $10^{-8}$  Hartree. We started the SCF calculations both from a closed-shell initial guess and an open-shell initial guess based on four unpaired electrons. In the 2c calculations, the initial wave function was chosen to be an eigenfunction of  $S_x$  or  $S_z$ , and the converged 2c wave function is thus aligned accordingly. Note that we assume periodicity along the  $x$  direction for one-dimensional systems [147]. Our unit cell consists of two platinum atoms and is indicated in Fig. 1(a). The cell parameter  $d$  was varied from 4.0 Å to 6.0 Å. All structures are specified in the Supplemental Material.

According to the restricted and unrestricted DFT calculations in Fig. 3(d)–3(f), no notable spin polarization occurs for unit cells with  $d$  smaller than 5.0 Å. Here, the spin expectation values are essentially zero. The most en-

ergetically favorable structure is found for  $d = 4.75$  Å in both scalar-relativistic and spin-orbit calculations. Apparently the impact of spin-orbit coupling on the geometric structure is small for this system. However, spin-orbit interaction has a large impact on the electronic band structures. For the 2c Kramers-restricted solution in Fig. 3(a), only two bands cross the Fermi level of  $\epsilon_F = 0$  eV. In contrast, seven and four bands cross the Fermi level for the Kramers-unrestricted solutions with the  $S_x$  and  $S_z$  alignments, respectively, see Fig. 3(b) and 3(c). For the latter two cases, many bands are split due to spin-orbit effects. Therefore, we find that spin-orbit interaction substantially affects the band structure for all spin configurations.

Furthermore, spin-orbit coupling is of relevance for the magnetic moment and the spin expectation value. The Pt chains transition into a magnetic state at  $d = 5.25$  Å without taking spin-orbit interaction into account, while spin-orbit effects change the transition geometry to  $d = 5.11$  Å for the  $S_x$  orientation and to  $d = 5.35$  Å for the  $S_z$  orientation. Additionally, the absolute values of the respective spin expectation values are sensitive towards relativistic effects. In the 1c UKS formalism, we find  $\langle S_z \rangle = 1.2$  for large cells, while the 2c calculations lead to  $\langle S_x \rangle = 1.0$  and  $\langle S_z \rangle = 0.85$ . Therefore, choosing the spin parallel to the periodic direction ( $x$  axis) notably affects the absolute spin expectation values and consequently the magnetic moments. In the spin-only approximation, the latter are obtained in units of Bohr's magneton  $\mu_B$  by doubling the spin expectation value. This results in  $1.2 \mu_B$  per atom for the linear chain with  $d > 5.5$  Å. Thus, our scalar-relativistic results are in excellent agreement with the previous study of Fernández-Rossier *et al.*, who predicted a magnetic transition at  $d = 5.2$  Å and a magnetic moment of  $1.2 \mu_B$  per atom [152] based on UKS PBE calculations with the GTO-based code CRYSTAL03. Note that these authors used one platinum atom per unit cell and hence the lattice spacing in their work has to be converted for comparison with our results. The findings are furthermore consistent with the studies of Delin and Tosatti [154] using the plane-wave code WIEN97.

## IV. SUMMARY AND OUTLOOK

We presented an efficient two-component procedure, which accounts for spin-orbit effects as well as for scalar-relativistic effects in a self-consistent manner. Relativistic effects are introduced with effective core potentials. Due to the use of Gaussian-type orbitals, our implementation is applicable to both molecular and periodic systems of any dimensionality.

We demonstrated the validity of our approach by calculating the ionization energy of heavy  $p$  elements, the electronic bulk band structure of gold and lead, band gaps of silver halide crystals, the cell and band structure of the InTe honeycomb system, as well as the geometry-dependent magnetic moment and spin polarizations of

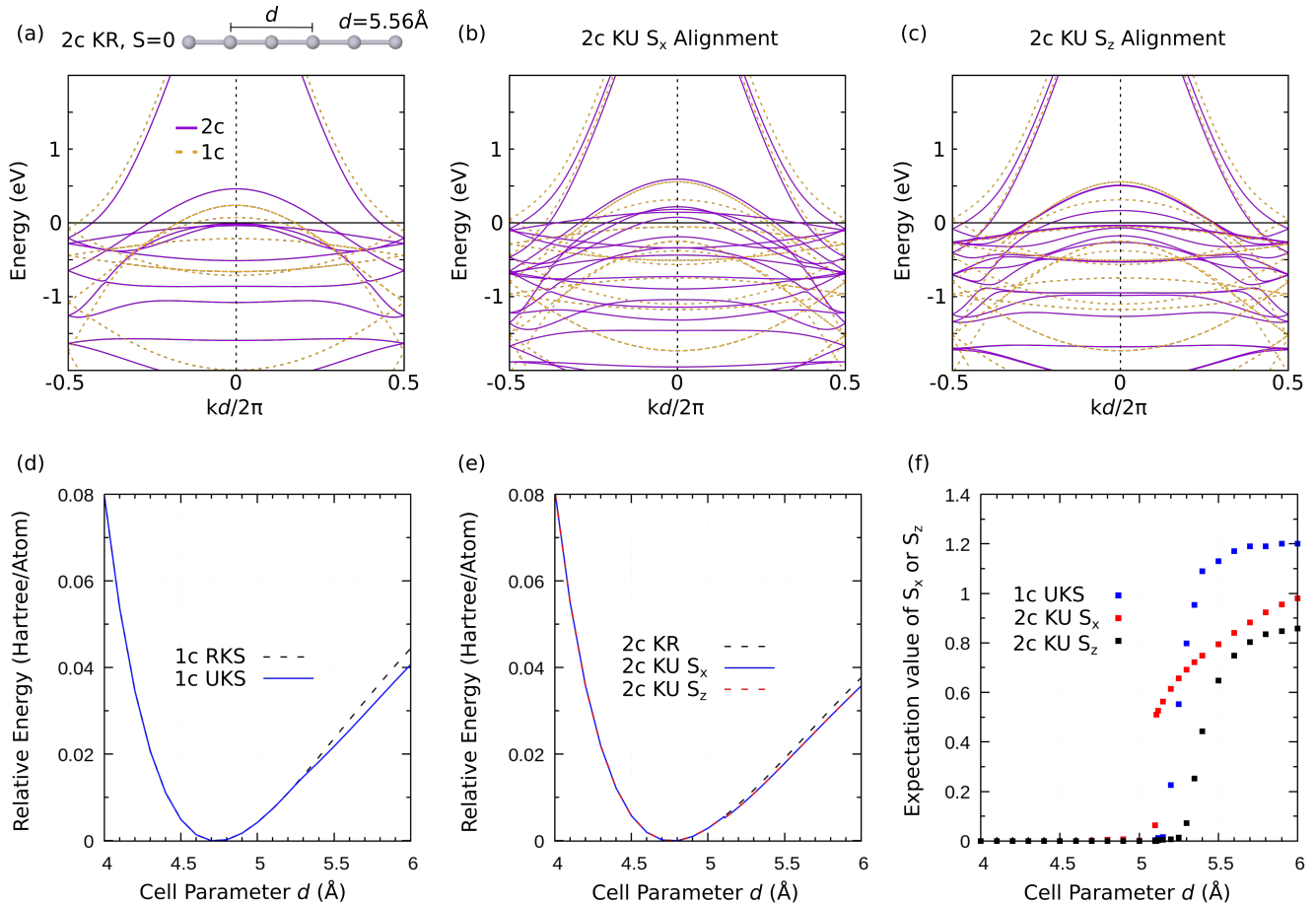


FIG. 3. (a)–(c) Electronic band structure in the FBZ for a linear platinum chain. The unit cell consists of two platinum atoms and is exemplarily shown in panel (a). The black vertical dashed line marks the  $\Gamma$  point of the FBZ. Scalar-relativistic results are presented in orange color, while the solid purple lines refer to calculations including spin–orbit interactions, see also panel (a). A closed-shell SCF solution and open-shell (magnetic) solutions in panels (b) and (c) are found. For the 2c calculations, two magnetic solutions with the spin aligned along the  $x$  axis, panel (b), or the  $z$  axis, panel (c), can be constructed. KR denotes the Kramers-restricted 2c solution, whereas KU  $S_x$  and KU  $S_z$  refer to the Kramers-unrestricted solutions with  $S_x$  alignment and  $S_z$  alignment. The expectation values of the respective spin components are 0.82 and 0.71, while those of the two other components vanished in the corresponding calculations. Note that we assume periodicity along the  $x$  direction for one-dimensional systems [147]. The open-shell solutions are energetically favored by about  $4 \cdot 10^{-3}$  Hartree (1c),  $1 \cdot 10^{-3}$  Hartree (2c  $S_x$  alignment), and  $1 \cdot 10^{-3}$  Hartree (2c  $S_z$  alignment). Calculations are performed with the PBE functional [97] and the dhf-TZVP-2c basis set [98]. (d) Dependence of the energy on the cell parameter in units of Hartree per atom for the 1c RKS and UKS calculations. (e) Dependence of the energy on the cell parameter in units of Hartree per atom for the 2c KR, 2c KU  $S_x$ , and 2c KU  $S_z$  calculations. (f) Expectation value of the spin component for the 1c UKS ( $S_z$ ), 2c KU  $S_x$ , and 2c KU  $S_z$  calculations. In the spin-only approximation, this corresponds to the magnetic moment in units of Bohr’s magneton  $\mu_B$  per atom.

linear platinum chains. In the process, we assessed the accuracy of the implementation by comparison with the plane-wave-based QUANTUM ESPRESSO program and other codes, showing excellent agreement.

Extension of this work is promising in multiple directions. In terms of density functional approximations, this covers the incorporation of Fock exchange [70] for (range-separated) hybrid functionals and the extension of the mGGA framework to account for the (paramagnetic) current density [39]. An extension to local hybrid functionals [155] may be useful to allow for a flexible admixture of Fock exchange [57, 156, 157] Additionally,

(local) relativistic all-electron approaches are necessary to study energetically low-lying states and the density in the vicinity of the nuclei [158, 159].

## SUPPLEMENTAL MATERIAL

Supplemental Material is available:

- Basis set study of silver halide crystals with non-relaxed structure,
- Density functional approximation study of silver

halide crystals with relaxed structures: Scalar-relativistic and spin-orbit results,

- Further results for the indium(I,III)-telluride two-dimensional honeycomb system
- All structures (coordinate input files) used in this work
  - Computation time
  - Ionization potentials of heavy  $p$ -elements
  - Band structures of three-dimensional gold and lead crystals
  - Band gaps of three-dimensional silver halide crystals
  - Indium(I,III)-telluride two-dimensional honeycomb structure
  - One-dimensional platinum chains

#### AUTHOR'S CONTRIBUTIONS

Y. J. Franzke and W. M. Schosser contributed equally to this work.

#### ACKNOWLEDGMENTS

We thank Christof Holzer (Karlsruhe), Marek Sierka (Jena), and Florian Weigend (Marburg) for stimulating discussions. Y.J.F. acknowledges TURBOMOLE GmbH for financial support.

#### DATA AVAILABILITY STATEMENT

The data that support the findings of this study are available within the article and its Supplemental Material.

- 
- [1] M. Dolg and X. Cao, Relativistic pseudopotentials: Their development and scope of applications, *Chem. Rev.* **112**, 403 (2012).
- [2] T. Saue, Relativistic Hamiltonians for chemistry: A primer, *ChemPhysChem* **12**, 3077 (2011).
- [3] J. Autschbach, Perspective: Relativistic effects, *J. Chem. Phys.* **136**, 150902 (2012).
- [4] P. Pyykkö, Relativistic effects in chemistry: More common than you thought, *Annu. Rev. Phys. Chem.* **63**, 45 (2012).
- [5] W. Liu, Essentials of relativistic quantum chemistry, *J. Chem. Phys.* **152**, 180901 (2020).
- [6] K. G. Dyall and K. Fægri Jr., *Introduction to Relativistic Quantum Chemistry* (Oxford University Press, New York, NY, USA, 2007).
- [7] M. Reiher and A. Wolf., *Relativistic Quantum Chemistry – The Fundamental Theory of Molecular Science*, 2nd ed. (Wiley-VCH, Weinheim, Germany, 2015).
- [8] W. Liu, ed., *Handbook of Relativistic Quantum Chemistry* (Springer, Berlin, Heidelberg, Germany, 2017).
- [9] P. Pyykkö, The physics behind chemistry and the periodic table, *Chem. Rev.* **112**, 371 (2012).
- [10] P. Schwerdtfeger, *Relativistic Electronic Structure Theory: Part 1. Fundamentals* (Elsevier, Amsterdam, The Netherlands, 2002).
- [11] P. Schwerdtfeger, *Relativistic Electronic Structure Theory: Part 2. Applications* (Elsevier, Amsterdam, The Netherlands, 2004).
- [12] S. Wilson, I. Grant, and B. L. Gyorffy, *The effects of relativity in atoms, molecules, and the solid state* (Springer, New York, NY, USA, 1991).
- [13] I. Grant, Relativistic electronic structure of atoms and molecules, in *Advances In Atomic, Molecular, and Optical Physics*, Vol. 32, edited by B. Bederson and A. Dalgarno (Academic Press, San Diego, CA, USA, 1994) pp. 169–186.
- [14] P. Pyykkö, Theoretical chemistry of gold. III, *Chem. Soc. Rev.* **37**, 1967 (2008).
- [15] P. Pyykko and J. P. Desclaux, Relativity and the periodic system of elements, *Acc. Chem. Res.* **12**, 276 (1979).
- [16] P. Pyykkö, Relativistic effects in structural chemistry, *Chem. Rev.* **88**, 563 (1988).
- [17] K. Ishizaka, M. Bahramy, H. Murakawa, M. Sakano, T. Shimojima, T. Sonobe, K. Koizumi, S. Shin, H. Miyahara, A. Kimura, K. Miyamoto, T. Okuda, H. Namatame, M. Taniguchi, R. Rita, N. Nagaosa, K. Kobayashi, Y. Murakami, R. Kumai, Y. Kaneko, Y. Onose, and Y. Tokura, Giant Rashba-type spin splitting in bulk BiTeI, *Nat. Mater.* **10**, 521 (2011).
- [18] J. Kübler, *Theory of Itinerant Electron Magnetism* (Oxford University Press, New York, NY, USA, 2000).
- [19] D. Pesin and L. Balents, Mott physics and band topology in materials with strong spin-orbit interaction, *Nat. Phys.* **6**, 376 (2010).
- [20] V. M. García-Suárez, D. Z. Manrique, C. J. Lambert, and J. Ferrer, Anisotropic magnetoresistance in atomic chains of iridium and platinum from first principles, *Phys. Rev. B* **79**, 060408 (2009).
- [21] M. Häfner, J. Viljas, and J. Cuevas, Theory of anisotropic magnetoresistance in atomic-sized ferromagnetic metal contacts, *Phys. Rev. B* **79**, 140410 (2009).
- [22] B. Hardrat, F. Freimuth, S. Heinze, and Y. Mokrousov, Conductance fingerprints of noncollinear magnetic states in single-atom contacts: A first-principles Wannier-functions study, *Phys. Rev. B* **86**, 165449 (2012).

- (2012).
- [23] D. Jacob, J. Fernández-Rossier, and J. J. Palacios, Anisotropic magnetoresistance in nanocontacts, *Phys. Rev. B* **77**, 165412 (2008).
- [24] S. Schmaus, A. Bagrets, Y. Nahas, T. K. Yamada, A. Bork, M. Bowen, E. Beaupaire, F. Evers, and W. Wulfhekel, Giant magnetoresistance through a single molecule, *Nat. Nanotechnol.* **6**, 185 (2011).
- [25] S. L. Kawahara, J. Lagoute, V. Repain, C. Chacon, Y. Girard, S. Rousset, A. Smogunov, and C. Barreateau, Large magnetoresistance through a single molecule due to a spin-split hybridized orbital, *Nano Lett.* **12**, 4558 (2012).
- [26] R. Hayakawa, M. A. Karimi, J. Wolf, T. Huhn, M. S. Zöllner, C. Herrmann, and E. Scheer, Large magnetoresistance in single-radical molecular junctions, *Nano Lett.* **16**, 4960 (2016).
- [27] F. Strigl, C. Espy, M. Bückle, E. Scheer, and T. Pietsch, Emerging magnetic order in platinum atomic contacts and chains, *Nat. Commun.* **6**, 1 (2015).
- [28] W. Kang, Y. Huang, X. Zhang, Y. Zhou, and W. Zhao, Skyrmion-electronics: An overview and outlook, *Proc. IEEE* **104**, 2040 (2016).
- [29] M. Heide, G. Bihlmayer, and S. Blügel, Dzyaloshinskii-Moriya interaction accounting for the orientation of magnetic domains in ultrathin films: Fe/W(110), *Phys. Rev. B* **78**, 140403 (2008).
- [30] M. Heide, G. Bihlmayer, and S. Blügel, Describing Dzyaloshinskii-Moriya spirals from first principles, *Physica B* **404**, 2678 (2009).
- [31] M. Z. Hasan and C. L. Kane, Colloquium: Topological insulators, *Rev. Mod. Phys.* **82**, 3045 (2010).
- [32] C. Pauly, G. Bihlmayer, M. Liebmann, M. Grob, A. Georgi, D. Subramaniam, M. R. Scholz, J. Sánchez-Barriga, A. Varykhalov, S. Blügel, O. Rader, and M. Morgenstern, Probing two topological surface bands of Sb<sub>2</sub>Te<sub>3</sub> by spin-polarized photoemission spectroscopy, *Phys. Rev. B* **86**, 235106 (2012).
- [33] M. Dolg, Relativistic effective core potentials, in *Relativistic Electronic Structure Theory*, Theoretical and Computational Chemistry, Vol. 11, edited by P. Schwerdtfeger (Elsevier, Amsterdam, The Netherlands, 2002) Chap. 14, pp. 793–862.
- [34] M. Dolg, Relativistic effective core potentials, in *Handbook of Relativistic Quantum Chemistry*, edited by W. Liu (Springer, Berlin, Heidelberg, 2017) Chap. 14, pp. 449–478.
- [35] C. Van Wüllen, Relativistic all-electron density functional calculations, *J. Comput. Chem.* **20**, 51 (1999).
- [36] C. Van Wüllen, Spin densities in two-component relativistic density functional calculations: Noncollinear versus collinear approach, *J. Comput. Chem.* **23**, 779 (2002).
- [37] M. K. Armbruster, F. Weigend, C. van Wüllen, and W. Klopper, Self-consistent treatment of spin-orbit interactions with efficient Hartree-Fock and density functional methods, *Phys. Chem. Chem. Phys.* **10**, 1748 (2008).
- [38] A. Baldes and F. Weigend, Efficient two-component self-consistent field procedures and gradients: implementation in TURBOMOLE and application to Au<sub>20</sub><sup>-</sup>, *Mol. Phys.* **111**, 2617 (2013).
- [39] C. Holzer, Y. J. Franzke, and A. Pausch, Current density functional framework for spin-orbit coupling, *J. Chem. Phys.* **157**, 204102 (2022).
- [40] J. E. Peralta, G. E. Scuseria, and M. J. Frisch, Non-collinear magnetism in density functional calculations, *Phys. Rev. B* **75**, 125119 (2007).
- [41] G. Scalmani and M. J. Frisch, A new approach to non-collinear spin density functional theory beyond the local density approximation, *J. Chem. Theory Comput.* **8**, 2193 (2012).
- [42] J. K. Desmarais, S. Komorovsky, J.-P. Flament, and A. Erba, Spin-orbit coupling from a two-component self-consistent approach. II. Non-collinear density functional theories, *J. Chem. Phys.* **154**, 204110 (2021).
- [43] C. D. Sherrill, D. E. Manolopoulos, T. J. Martínez, and A. Michaelides, Electronic structure software, *J. Chem. Phys.* **153**, 070401 (2020).
- [44] Developers' version of TURBOMOLE V7.7 (2022), a development of University of Karlsruhe and Forschungszentrum Karlsruhe GmbH, 1989-2007, TURBOMOLE GmbH, since 2007; available from <https://www.turbomole.org> (retrieved May 4, 2023).
- [45] R. Ahlrichs, M. Bär, M. Häser, H. Horn, and C. Kölmel, Electronic structure calculations on workstation computers: The program system turbomole, *Chem. Phys. Lett.* **162**, 165 (1989).
- [46] F. Furche, R. Ahlrichs, C. Hättig, W. Klopper, M. Sierka, and F. Weigend, Turbomole, *Wiley Interdiscip. Rev.: Comput. Mol. Sci.* **4**, 91 (2014).
- [47] S. G. Balasubramani, G. P. Chen, S. Coriani, M. Diedenhofen, M. S. Frank, Y. J. Franzke, F. Furche, R. Grotjahn, M. E. Harding, C. Hättig, A. Hellweg, B. Helmich-Paris, C. Holzer, U. Huniar, M. Kaupp, A. Marefat Khah, S. Karbalaei Khani, T. Müller, F. Mack, B. D. Nguyen, S. M. Parker, E. Perlt, D. Rapoport, K. Reiter, S. Roy, M. Rückert, G. Schmitz, M. Sierka, E. Tapavicza, D. P. Tew, C. van Wüllen, V. K. Voora, F. Weigend, A. Wodyński, and J. M. Yu, TURBOMOLE: Modular program suite for *ab initio* quantum-chemical and condensed-matter simulations, *J. Chem. Phys.* **152**, 184107 (2020).
- [48] J. K. Desmarais, J.-P. Flament, and A. Erba, Spin-orbit coupling in periodic systems with broken time-reversal symmetry: Formal and computational aspects, *Phys. Rev. B* **101**, 235142 (2020).
- [49] J. K. Desmarais, J.-P. Flament, and A. Erba, Adiabatic connection in spin-current density functional theory, *Phys. Rev. B* **102**, 235118 (2020).
- [50] F. Bodo, J. K. Desmarais, and A. Erba, Spin current density functional theory of Weyl semimetals, *Phys. Rev. B* **105**, 125108 (2022).
- [51] A. Erba, J. K. Desmarais, S. Casassa, B. Civalieri, L. Donà, I. J. Bush, B. Searle, L. Maschio, L. Edith-Daga, A. Cossard, C. Ribaldone, E. Ascricchi, N. L. Marana, J.-P. Flament, and B. Kirtman, CRYSTAL23: A program for computational solid state physics and chemistry, *J. Chem. Theory Comput.* (2022).
- [52] N. Mardirossian and M. Head-Gordon, Thirty years of density functional theory in computational chemistry: an overview and extensive assessment of 200 density functionals, *Mol. Phys.* **115**, 2315 (2017).
- [53] P. Hao, J. Sun, B. Xiao, A. Ruzsinszky, G. I. Csonka, J. Tao, S. Glindmeyer, and J. P. Perdew, Performance of meta-GGA functionals on general main group thermochemistry, kinetics, and noncovalent interactions, *J. Chem. Theory Comput.* **9**, 355 (2013).
- [54] Y. Mo, R. Car, V. N. Staroverov, G. E. Scuseria, and J. Tao, Assessment of the Tao-Mo nonempirical semilo-

- cal density functional in applications to solids and surfaces, *Phys. Rev. B* **95**, 035118 (2017).
- [55] L. Goerigk, A. Hansen, C. Bauer, S. Ehrlich, A. Najibi, and S. Grimme, A look at the density functional theory zoo with the advanced GMTKN55 database for general main group thermochemistry, kinetics and noncovalent interactions, *Phys. Chem. Chem. Phys.* **19**, 32184 (2017).
- [56] T. Aschebrock and S. Kümmel, Ultranonlocality and accurate band gaps from a meta-generalized gradient approximation, *Phys. Rev. Res.* **1**, 033082 (2019).
- [57] C. Holzer, Y. J. Franzke, and M. Kehn, Assessing the accuracy of local hybrid density functional approximations for molecular response properties, *J. Chem. Theory Comput.* **17**, 2928 (2021).
- [58] Y. J. Franzke and J. M. Yu, Hyperfine coupling constants in local exact two-component theory, *J. Chem. Theory Comput.* **18**, 323 (2022).
- [59] Y. J. Franzke and J. M. Yu, Quasi-relativistic calculation of EPR  $g$  tensors with derivatives of the decoupling transformation, gauge-including atomic orbitals, and magnetic balance, *J. Chem. Theory Comput.* **18**, 2246 (2022).
- [60] A. D. Becke, Perspective: Fifty years of density-functional theory in chemical physics, *J. Chem. Phys.* **140**, 18A301 (2014).
- [61] A. D. Becke, Density-functional theory vs density-functional fits, *J. Chem. Phys.* **156**, 214101 (2022).
- [62] P. Borlido, T. Aull, A. W. Huran, F. Tran, M. A. L. Marques, and S. Botti, Large-scale benchmark of exchange–correlation functionals for the determination of electronic band gaps of solids, *J. Chem. Theory Comput.* **15**, 5069 (2019).
- [63] A. Ghosh, S. Jana, T. Rauch, F. Tran, M. A. L. Marques, S. Botti, L. A. Constantin, M. K. Niranjan, and P. Samal, Efficient and improved prediction of the band offsets at semiconductor heterojunctions from meta-GGA density functionals: A benchmark study, *J. Chem. Phys.* **157**, 124108 (2022).
- [64] P. Kovás, F. Tran, P. Blaha, and G. K. H. Madsen, What is the optimal mGGA exchange functional for solids?, *J. Chem. Phys.* **157**, 094110 (2022).
- [65] A. M. Burow, M. Sierka, and F. Mohamed, Resolution of identity approximation for the Coulomb term in molecular and periodic systems, *J. Chem. Phys.* **131**, 214101 (2009).
- [66] A. M. Burow and M. Sierka, Linear scaling hierarchical integration scheme for the exchange-correlation term in molecular and periodic systems, *J. Chem. Theory Comput.* **7**, 3097 (2011).
- [67] R. Łazarski, A. M. Burow, and M. Sierka, Density functional theory for molecular and periodic systems using density fitting and continuous fast multipole methods, *J. Chem. Theory Comput.* **11**, 3029 (2015).
- [68] R. Łazarski, A. M. Burow, L. Grajciar, and M. Sierka, Density functional theory for molecular and periodic systems using density fitting and continuous fast multipole method: Analytical gradients, *J. Comput. Chem.* **37**, 2518 (2016).
- [69] L. Grajciar, Low-memory iterative density fitting, *J. Comput. Chem.* **36**, 1521 (2015).
- [70] A. Irmeler, A. M. Burow, and F. Pauly, Robust periodic Fock exchange with atom-centered Gaussian basis sets, *J. Chem. Theory Comput.* **14**, 4567 (2018).
- [71] A. Irmeler and F. Pauly, Multipole-based distance-dependent screening of Coulomb integrals, *J. Chem. Phys.* **151**, 084111 (2019).
- [72] S. Grimme, J. Antony, S. Ehrlich, and H. Krieg, A consistent and accurate ab initio parametrization of density functional dispersion correction (DFT-D) for the 94 elements H-Pu, *J. Chem. Phys.* **132**, 154104 (2010).
- [73] S. Grimme, S. Ehrlich, and L. Goerigk, Effect of the damping function in dispersion corrected density functional theory, *J. Comput. Chem.* **32**, 1456 (2011).
- [74] P. M. Gill, B. G. Johnson, and J. A. Pople, A standard grid for density functional calculations, *Chem. Phys. Lett.* **209**, 506 (1993).
- [75] M. Becker and M. Sierka, Density functional theory for molecular and periodic systems using density fitting and continuous fast multipole method: Stress tensor, *J. Comput. Chem.* **40**, 2563 (2019).
- [76] K. N. Kudin and G. E. Scuseria, Analytic stress tensor with the periodic fast multipole method, *Phys. Rev. B* **61**, 5141 (2000).
- [77] T. Bučko, J. Hafner, and J. G. Ángyán, Geometry optimization of periodic systems using internal coordinates, *J. Chem. Phys.* **122**, 124508 (2005).
- [78] K. Doll, Analytical stress tensor and pressure calculations with the crystal code, *Mol. Phys.* **108**, 223 (2010).
- [79] F. Knuth, C. Carbogno, V. Atalla, V. Blum, and M. Scheffler, All-electron formalism for total energy strain derivatives and stress tensor components for numeric atom-centered orbitals, *Comput. Phys. Commun.* **190**, 33 (2015).
- [80] H. B. Schlegel, Geometry optimization, *Wiley Interdiscip. Rev.: Comput. Mol. Sci.* **1**, 790 (2011).
- [81] P. Pulay, Analytical derivatives, forces, force constants, molecular geometries, and related response properties in electronic structure theory, *Wiley Interdiscip. Rev.: Comput. Mol. Sci.* **4**, 169 (2014).
- [82] P. Pulay, Ab initio calculation of force constants and equilibrium geometries in polyatomic molecules, *Mol. Phys.* **17**, 197 (1969).
- [83] L. Versluis and T. Ziegler, The determination of molecular structures by density functional theory. the evaluation of analytical energy gradients by numerical integration, *J. Chem. Phys.* **88**, 322 (1988).
- [84] J. A. Pople, P. M. Gill, and B. G. Johnson, Kohn–Sham density-functional theory within a finite basis set, *Chem. Phys. Lett.* **199**, 557 (1992).
- [85] B. G. Johnson, P. M. W. Gill, and J. A. Pople, The performance of a family of density functional methods, *J. Chem. Phys.* **98**, 5612 (1993).
- [86] J. Baker, J. Andzelm, A. Scheiner, and B. Delley, The effect of grid quality and weight derivatives in density functional calculations, *J. Chem. Phys.* **101**, 8894 (1994).
- [87] R. Stratmann, G. E. Scuseria, and M. J. Frisch, Achieving linear scaling in exchange-correlation density functional quadratures, *Chem. Phys.* **257**, 213 (1996).
- [88] M. Tobita, S. Hirata, and R. J. Bartlett, The analytical energy gradient scheme in the gaussian based hartree–fock and density functional theory for two-dimensional systems using the fast multipole method, *J. Chem. Phys.* **118**, 5776 (2003).
- [89] L. E. McMurchie and E. R. Davidson, Calculation of integrals over ab initio pseudopotentials, *J. Comput. Phys.* **44**, 289 (1981).



- [90] R. M. Pitzer and N. W. Winter, Spin-orbit (core) and core potential integrals, *Int. J. Quantum Chem.* **40**, 773 (1991).
- [91] OpenMP Architecture Review Boards, OpenMP API shared-memory parallel programming, <https://www.openmp.org> (retrieved December 20, 2022).
- [92] C. Holzer and Y. J. Franzke, OpenMP versions of `ridft`, `rdgrad`, and `egrad` with contributions to `mpshift`, `dscf`, and `grad`; improved OpenMP versions of `aoforce` and `escf`, released with TURBOMOLE V7.4 and further improved in TURBOMOLE V7.5.
- [93] P. Pulay, Convergence acceleration of iterative sequences. The case of SCF iteration, *Chem. Phys. Lett.* **73**, 393 (1980).
- [94] M. A. L. Marques, M. J. T. Oliveira, and T. Burnus, LIBXC: A library of exchange and correlation functionals for density functional theory, *Comput. Phys. Commun.* **183**, 2272 (2012).
- [95] S. Lehtola, C. Steigemann, M. J. T. Oliveira, and M. A. L. Marques, Recent developments in LIBXC – a comprehensive library of functionals for density functional theory, *SoftwareX* **7**, 1 (2018).
- [96] LIBXC, Version 6.0.0, available from <https://www.tddft.org/programs/libxc/> (retrieved August 16, 2022).
- [97] J. P. Perdew, K. Burke, and M. Ernzerhof, Generalized Gradient Approximation Made Simple, *Phys. Rev. Lett.* **77**, 3865 (1996).
- [98] F. Weigend and A. Baldes, Segmented contracted basis sets for one- and two-component Dirac–Fock effective core potentials, *J. Chem. Phys.* **133**, 174102 (2010).
- [99] O. Treutler, *Entwicklung und Anwendung von Dichtefunktionalmethoden*, Dissertation (Dr. rer. nat.), University of Karlsruhe (TH), Germany (1995).
- [100] O. Treutler and R. Ahlrichs, Efficient molecular numerical integration schemes, *J. Chem. Phys.* **102**, 346 (1995).
- [101] B. Metz, H. Stoll, and M. Dolg, Small-core multiconfiguration-Dirac–Hartree–Fock-adjusted pseudopotentials for post-*d* main group elements: Application to PbH and PbO, *J. Chem. Phys.* **113**, 2563 (2000).
- [102] K. Eichkorn, O. Treutler, H. Öhm, M. Häser, and R. Ahlrichs, Auxiliary Basis Sets to Approximate Coulomb Potentials, *Chem. Phys. Lett.* **242**, 283 (1995).
- [103] K. Eichkorn, F. Weigend, O. Treutler, and R. Ahlrichs, Auxiliary basis sets for main row atoms and transition metals and their use to approximate Coulomb potentials, *Theor. Chem. Acc.* **97**, 119 (1997).
- [104] F. Weigend, M. Kattannek, and R. Ahlrichs, Approximated electron repulsion integrals: Cholesky decomposition versus resolution of the identity methods, *J. Chem. Phys.* **130**, 164106 (2009).
- [105] J. E. Huheey, E. A. Keiter, and R. L. Keiter, *Inorganic Chemistry: Principles of Structure and Reactivity*, 4th ed. (HarperCollins, New York, NY, USA, 1994).
- [106] C. E. Housecroft and A. G. Sharpe, *Inorganic Chemistry*, 4th ed. (Pearson, Harlow, United Kingdom, 2012).
- [107] Y. Ralchenko, F. Jou, D. Kelleher, A. Kramida, A. Musgrove, J. Reader, W. Wiese, and K. Olsen, NIST atomic spectra database (version 3.1.0) (2006), retrived March 27, 2023.
- [108] P. Giannozzi, O. Baseggio, P. Bonfà, D. Brunato, R. Car, I. Carnimeo, C. Cavazzoni, S. de Gironcoli, P. Delugas, F. Ferrari Ruffino, A. Ferretti, N. Marzari, I. Timrov, A. Urru, and S. Baroni, Quantum ESPRESSO toward the exascale, *J. Chem. Phys.* **152**, 154105 (2020).
- [109] WolframResearch, ElementData, <https://reference.wolfram.com/language/ref/ElementData.html>, (accessed December 2, 2021).
- [110] D. Figgen, K. A. Peterson, M. Dolg, and H. Stoll, Energy-consistent pseudopotentials and correlation consistent basis sets for the 5*d* elements Hf–Pt, *J. Chem. Phys.* **130**, 164108 (2009).
- [111] G. Kresse and J. Furthmüller, Efficiency of ab-initio total energy calculations for metals and semiconductors using a plane-wave basis set, *Comput. Mater. Sci.* **6**, 15 (1996).
- [112] W. Sachtler, G. Dorgelo, and A. Holscher, The work function of gold, *Surf. Sci.* **5**, 221 (1966).
- [113] P. A. Anderson and A. L. Hunt, Work function of lead, *Phys. Rev.* **102**, 367 (1956).
- [114] J. E. Peralta, J. Uddin, and G. E. Scuseria, Scalar relativistic all-electron density functional calculations on periodic systems, *J. Chem. Phys.* **122**, 084108 (2005).
- [115] R. Zhao, Y. Zhang, Y. Xiao, and W. Liu, Exact two-component relativistic energy band theory and application, *J. Chem. Phys.* **144**, 044105 (2016).
- [116] M. Kadek, M. Repisky, and K. Ruud, All-electron fully relativistic Kohn–Sham theory for solids based on the Dirac–Coulomb Hamiltonian and Gaussian-type functions, *Phys. Rev. B* **99**, 205103 (2019).
- [117] C.-N. Yeh, A. Shee, Q. Sun, E. Gull, and D. Zgid, Relativistic self-consistent *GW*: Exact two-component formalism with one-electron approximation for solids, *Phys. Rev. B* **106**, 085121 (2022).
- [118] F. Weigend and R. Ahlrichs, Balanced basis sets of split valence, triple zeta valence and quadruple zeta valence quality for H to Rn: Design and assessment of accuracy, *Phys. Chem. Chem. Phys.* **7**, 3297 (2005).
- [119] R. Ahlrichs and K. May, Contracted all-electron gaussian basis sets for atoms Rb to Xe, *Phys. Chem. Chem. Phys.* **2**, 943 (2000).
- [120] D. Figgen, G. Rauhut, M. Dolg, and H. Stoll, Energy-consistent pseudopotentials for group 11 and 12 atoms: adjustment to multi-configuration Dirac–Hartree–Fock data, *Chem. Phys.* **311**, 227 (2005).
- [121] K. A. Peterson, B. C. Shepler, D. Figgen, and H. Stoll, On the spectroscopic and thermochemical properties of ClO, BrO, IO, and their anions, *J. Phys. Chem. A* **110**, 13877 (2006).
- [122] M. F. Peintinger, D. V. Oliveira, and T. Bredow, Consistent Gaussian basis sets of triple-zeta valence with polarization quality for solid-state calculations, *J. Comput. Chem.* **34**, 451 (2013).
- [123] K. G. Dyall, Relativistic quadruple-zeta and revised triple-zeta and double-zeta basis sets for the 4*p*, 5*p*, and 6*p* elements, *Theor. Chem. Acc.* **115**, 441 (2006).
- [124] K. G. Dyall, Relativistic double-zeta, triple-zeta, and quadruple-zeta basis sets for the 4*d* elements Y–Cd, *Theor. Chem. Acc.* **117**, 483 (2007).
- [125] C. R. Berry, Physical defects in silver halides, *Phys. Rev.* **97**, 676 (1955).
- [126] W. Hidshaw, J. T. Lewis, and C. V. Briscoe, Elastic constants of silver chloride from 4.2 to 300°K, *Phys. Rev.* **163**, 876 (1967).
- [127] D. Vogel, P. Krüger, and J. Pollmann, Ab initio electronic structure of silver halides calculated with self-interaction and relaxation-corrected pseudopotentials,

- Phys. Rev. B **58**, 3865 (1998).
- [128] A. H. Sommer, *Photoemissive Materials: Preparation, Properties and Uses*, 1st ed. (John Wiley & Sons, New York, NY, USA, 1986) Chap. 3, p. 21.
- [129] P. Wang, B. Huang, X. Zhang, X. Qin, H. Jin, Y. Dai, Z. Wang, J. Wei, J. Zhan, S. Wang, J. Wang, and M.-H. Whangbo, Highly efficient visible-light plasmonic photocatalyst Ag@AgBr, *Chem. Eur. J.* **15**, 1821 (2009).
- [130] F. Bassani, R. S. Knox, and W. B. Fowler, Band structure and electronic properties of AgCl and AgBr, *Phys. Rev.* **137**, A1217 (1965).
- [131] G. Piermarini and C. Weir, A diamond cell for X-ray diffraction studies at high pressures, *J. Res. Natl. Bur. Stan., Sec. A* **66**, 325 (1962).
- [132] S. Ves, D. Glötzel, M. Cardona, and H. Overhof, Pressure dependence of the optical properties and the band structure of the copper and silver halides, *Phys. Rev. B* **24**, 3073 (1981).
- [133] J. C. Slater, A simplification of the Hartree–Fock method, *Phys. Rev.* **81**, 385 (1951).
- [134] S. H. Vosko, L. Wilk, and M. Nusair, Accurate spin-dependent electron liquid correlation energies for local spin density calculations: a critical analysis, *Can. J. Phys.* **58**, 1200 (1980).
- [135] J. P. Perdew, A. Ruzsinszky, G. I. Csonka, O. A. Vydrov, G. E. Scuseria, L. A. Constantin, X. Zhou, and K. Burke, Restoring the Density-Gradient Expansion for Exchange in Solids and Surfaces, *Phys. Rev. Lett.* **100**, 136406 (2008).
- [136] J. Tao, J. P. Perdew, V. N. Staroverov, and G. E. Scuseria, Climbing the Density Functional Ladder: Nonempirical Meta-Generalized Gradient Approximation Designed for Molecules and Solids, *Phys. Rev. Lett.* **91**, 146401 (2003).
- [137] J. P. Perdew, A. Ruzsinszky, G. I. Csonka, L. A. Constantin, and J. Sun, Workhorse Semilocal Density Functional for Condensed Matter Physics and Quantum Chemistry, *Phys. Rev. Lett.* **103**, 026403 (2009).
- [138] J. P. Perdew, A. Ruzsinszky, G. I. Csonka, L. A. Constantin, and J. Sun, Erratum: Workhorse Semilocal Density Functional for Condensed Matter Physics and Quantum Chemistry [Phys. Rev. Lett. 103, 026403 (2009)], *Phys. Rev. Lett.* **106**, 179902 (2011).
- [139] J. Tao and Y. Mo, Accurate Semilocal Density Functional for Condensed-Matter Physics and Quantum Chemistry, *Phys. Rev. Lett.* **117**, 073001 (2016).
- [140] J. P. Perdew, S. Kurth, A. Zupan, and P. Blaha, Accurate Density Functional with Correct Formal Properties: A Step Beyond the Generalized Gradient Approximation, *Phys. Rev. Lett.* **82**, 2544 (1999).
- [141] J. W. Furness, A. D. Kaplan, J. Ning, J. P. Perdew, and J. Sun, Accurate and numerically efficient r<sup>2</sup>SCAN meta-generalized gradient approximation, *J. Phys. Chem. Lett.* **11**, 8208 (2020).
- [142] J. W. Furness, A. D. Kaplan, J. Ning, J. P. Perdew, and J. Sun, Correction to “Accurate and numerically efficient r<sup>2</sup>SCAN meta-generalized gradient approximation”, *J. Phys. Chem. Lett.* **11**, 9248 (2020).
- [143] Minor deviations from the fcc structure were removed by symmetrization. This changed the energy by less than  $3 \cdot 10^{-4}$  Hartrees or less than 1 kJ/mol. Typically, changes are below  $10^{-5}$  Hartrees.
- [144] A. Patra, S. Jana, L. A. Constantin, and P. Samal, Efficient yet accurate dispersion-corrected semilocal exchange–correlation functionals for non-covalent interactions, *J. Chem. Phys.* **153**, 084117 (2020).
- [145] S. Ehlert, U. Huniar, J. Ning, J. W. Furness, J. Sun, A. D. Kaplan, J. P. Perdew, and J. G. Brandenburg, r<sup>2</sup>SCAN-D4: Dispersion corrected meta-generalized gradient approximation for general chemical applications, *J. Chem. Phys.* **154**, 061101 (2021).
- [146] J. Shang, L. Pan, X. Wang, J. Li, H.-X. Deng, and Z. Wei, Tunable electronic and optical properties of InSe/InTe van der Waals heterostructures toward optoelectronic applications, *J. Mater. Chem. C* **6**, 7201 (2018).
- [147] Manual of TURBOMOLE V7.7 (2022), a development of University of Karlsruhe and Forschungszentrum Karlsruhe GmbH, 1989-2007, TURBOMOLE GmbH, since 2007; available from <https://www.turbomole.org/turbomole/turbomole-documentation/> (retrieved May 4, 2023).
- [148] R. H. M. Smit, C. Untiedt, A. I. Yanson, and J. M. van Ruitenbeek, Common Origin for Surface Reconstruction and the Formation of Chains of Metal Atoms, *Phys. Rev. Lett.* **87**, 266102 (2001).
- [149] V. M. García-Suárez, A. R. Rocha, S. W. Bailey, C. J. Lambert, S. Cito, and J. Ferrer, Conductance Oscillations in Zigzag Platinum Chains, *Phys. Rev. Lett.* **95**, 256804 (2005).
- [150] A. Delin and E. Tosatti, Magnetic phenomena in 5d transition metal nanowires, *Phys. Rev. B* **68**, 144434 (2003).
- [151] T. Nautiyal, T. H. Rho, and K. S. Kim, Nanowires for spintronics: A study of transition-metal elements of groups 8–10, *Phys. Rev. B* **69**, 193404 (2004).
- [152] J. Fernández-Rossier, D. Jacob, C. Untiedt, and J. J. Palacios, Transport in magnetically ordered Pt nanocontacts, *Phys. Rev. B* **72**, 224418 (2005).
- [153] A. Smogunov, A. Dal Corso, A. Delin, R. Weht, and E. Tosatti, Colossal magnetic anisotropy of monatomic free and deposited platinum nanowires, *Nat. Nanotechnol.* **3**, 22 (2008).
- [154] A. Delin and E. Tosatti, Emerging magnetism in platinum nanowires, *Surf. Sci.* **566–568**, 262 (2004).
- [155] J. Jaramillo, G. E. Scuseria, and M. Ernzerhof, Local hybrid functionals, *J. Chem. Phys.* **118**, 1068 (2003).
- [156] C. Holzer and Y. J. Franzke, A local hybrid exchange functional approximation from first principles, *J. Chem. Phys.* **157**, 034108 (2022).
- [157] P. Plessow and F. Weigend, Seminumerical calculation of the Hartree–Fock exchange matrix: Application to two-component procedures and efficient evaluation of local hybrid density functionals, *J. Comput. Chem.* **33**, 810 (2012).
- [158] D. Peng, N. Middendorff, F. Weigend, and M. Reiher, An efficient implementation of two-component relativistic exact-decoupling methods for large molecules, *J. Chem. Phys.* **138**, 184105 (2013).
- [159] Y. J. Franzke, N. Middendorff, and F. Weigend, Efficient implementation of one- and two-component analytical energy gradients in exact two-component theory, *J. Chem. Phys.* **148**, 104410 (2018).

# Supplemental Material: Self-Consistent and Efficient Treatment of Relativistic Effects with Periodic Density Functional Methods: Energies, Gradients, and Stress Tensors

Yannick J. Franzke,<sup>1</sup> Werner M. Schosser,<sup>2</sup> and Fabian Pauly<sup>2,\*</sup>

<sup>1</sup>*Fachbereich Chemie, Philipps-Universität Marburg,  
Hans-Meerwein-Str. 4, 35032 Marburg, Germany*<sup>†</sup>

<sup>2</sup>*Institute of Physics and Centre for Advanced Analytics and Predictive Sciences,  
University of Augsburg, Universitätsstr. 1, 86159 Augsburg, Germany*<sup>†</sup>

(Dated: May 5, 2023)

## CONTENTS

I. Basis Set Study of Silver Halide Crystals with Non-Relaxed Structure	2
II. Density Functional Approximation Study of Silver Halide Crystals with Relaxed Structures: Scalar-Relativistic and Spin-Orbit Results	5
III. Further Results for the Indium(I,III)-Telluride Two-Dimensional Honeycomb System	8
IV. Structures	9
A. Computation Times	9
B. Ionization Potentials of Heavy $p$ -Elements	10
C. Band Structures of Three-Dimensional Gold and Lead Crystals	11
D. Band Gaps of Three-Dimensional Silver Halide Crystals	12
E. Indium(I,III)-Telluride Two-Dimensional Honeycomb Structure	31
F. One-Dimensional Platinum Chains	32
References	36

---

\* fabian.pauly@uni-a.de

<sup>†</sup> Y.J.F. and W.M.S. contributed equally to this work

# I. BASIS SET STUDY OF SILVER HALIDE CRYSTALS WITH NON-RELAXED STRUCTURE

TABLE I. Energy band gaps (in eV) of three-dimensional AgCl (lattice constant  $a = 5.612 \text{ \AA}$ , rocksalt structure [1]) for high symmetry points of the FBZ. The local spin density approximation (LSDA) is represented by the S-VWN (III) functional [2, 3], whereas PBE [4] and PBEsol [5] serve as examples for generalized gradient approximations (GGAs). *meta*-GGAs are included through the TPSS [6], revTPSS [7, 8], Tao–Mo [9], PKZB [10], and r<sup>2</sup>SCAN [11, 12] approximations. Note that we use LIBXC [13–15] for the PBEsol, revTPSS, Tao–Mo, PKZB, and r<sup>2</sup>SCAN functionals. The dhf-SVP and dhf-TZVP basis sets are employed [16].

	One-Component				Two-Component			
	L–L	$\Gamma$ – $\Gamma$	X–X	L– $\Gamma$	L–L	$\Gamma$ – $\Gamma$	X–X	L– $\Gamma$
dhf-SVP	L–L	$\Gamma$ – $\Gamma$	X–X	L– $\Gamma$	L–L	$\Gamma$ – $\Gamma$	X–X	L– $\Gamma$
S-VWN (III)	4.30	2.83	3.90	0.59	4.25	2.70	3.73	0.54
PBE	4.62	3.11	4.16	0.91	4.57	2.94	3.99	0.86
PBEsol	4.38	2.95	4.02	0.72	4.33	2.78	3.85	0.67
TPSS	4.65	3.16	4.29	1.03	4.60	3.00	4.12	0.98
revTPSS	4.52	3.10	4.27	0.96	4.46	2.93	4.10	0.90
Tao–Mo	4.38	3.12	4.36	1.03	4.33	2.96	4.20	0.97
PKZB	4.61	3.29	4.42	1.22	4.56	3.14	4.27	1.17
r <sup>2</sup> SCAN	5.11	3.64	4.71	1.47	5.06	3.47	4.55	1.41
dhf-TZVP	L–L	$\Gamma$ – $\Gamma$	X–X	L– $\Gamma$	L–L	$\Gamma$ – $\Gamma$	X–X	L– $\Gamma$
S-VWN (III)	4.09	2.77	3.79	0.54	4.04	2.68	3.62	0.49
PBE	4.37	3.07	4.03	0.85	4.32	2.90	3.86	0.80
PBEsol	4.16	2.91	3.90	0.66	4.11	2.75	3.72	0.61
TPSS	4.39	3.11	4.15	0.94	4.33	2.94	3.99	0.89
revTPSS	4.28	3.04	4.14	0.87	4.23	2.88	3.97	0.82
Tao–Mo	4.21	3.07	4.23	0.95	4.15	2.92	4.07	0.90
PKZB	4.44	3.26	4.29	1.17	4.39	3.11	4.14	1.11
r <sup>2</sup> SCAN	4.87	3.59	4.57	1.38	4.82	3.42	4.41	1.33

TABLE II. Energy band gaps (in eV) of three-dimensional AgBr (lattice constant  $a = 5.843 \text{ \AA}$ , rocksalt structure [1]) for high symmetry points of the FBZ. The local spin density approximation (LSDA) is represented by the S-VWN (III) functional [2, 3], whereas PBE [4] and PBEsol [5] serve as examples for generalized gradient approximations (GGAs). *meta*-GGAs are included through the TPSS [6], revTPSS [7, 8], Tao–Mo [9], PKZB [10], and r<sup>2</sup>SCAN [11, 12] approximations. Note that we use LIBXC [13–15] for the PBEsol, revTPSS, Tao–Mo, PKZB, and r<sup>2</sup>SCAN functionals. The dhf-SVP and dhf-TZVP basis sets are employed [16].

	One-Component				Two-Component			
	L–L	$\Gamma$ – $\Gamma$	X–X	L– $\Gamma$	L–L	$\Gamma$ – $\Gamma$	X–X	L– $\Gamma$
dhf-SVP	L–L	$\Gamma$ – $\Gamma$	X–X	L– $\Gamma$	L–L	$\Gamma$ – $\Gamma$	X–X	L– $\Gamma$
S-VWN (III)	3.81	2.34	3.47	0.54	3.76	2.33	3.31	0.50
PBE	4.07	2.64	3.70	0.86	4.02	2.64	3.54	0.82
PBEsol	3.87	2.49	3.57	0.68	3.82	2.48	3.41	0.64
TPSS	4.08	2.85	3.82	1.00	4.04	2.85	3.67	0.95
revTPSS	4.01	2.87	3.80	0.99	3.96	2.86	3.65	0.94
Tao–Mo	3.97	2.94	3.91	1.11	3.92	2.93	3.76	1.06
PKZB	4.14	3.03	3.96	1.23	4.09	3.03	3.81	1.19
r <sup>2</sup> SCAN	4.59	3.30	4.24	1.46	4.54	3.30	4.09	1.41
dhf-TZVP	L–L	$\Gamma$ – $\Gamma$	X–X	L– $\Gamma$	L–L	$\Gamma$ – $\Gamma$	X–X	L– $\Gamma$
S-VWN (III)	3.71	2.32	3.42	0.51	3.67	2.31	3.26	0.47
PBE	3.96	2.62	3.63	0.81	3.91	2.62	3.48	0.77
PBEsol	3.77	2.47	3.51	0.64	3.72	2.46	3.35	0.60
TPSS	3.99	2.83	3.75	0.95	3.94	2.82	3.60	0.90
revTPSS	3.92	2.83	3.73	0.92	3.87	2.82	3.58	0.88
Tao–Mo	3.89	2.89	3.83	1.04	3.84	2.88	3.68	0.99
PKZB	4.07	3.00	3.89	1.18	4.02	2.99	3.74	1.13
r <sup>2</sup> SCAN	4.48	3.27	4.16	1.40	4.43	3.27	4.01	1.36

TABLE III. Energy band gaps (in eV) of three-dimensional AgI (lattice constant  $a = 6.169 \text{ \AA}$ , rocksalt structure [1]) for high symmetry points of the FBZ. The local spin density approximation (LSDA) is represented by the S-VWN (III) functional, [2, 3] whereas PBE [4] and PBEsol [5] serve as examples for generalized gradient approximations (GGAs). *meta*-GGAs are included through the TPSS [6], revTPSS [7, 8], Tao–Mo [9], PKZB [10], and r<sup>2</sup>SCAN [11, 12] approximations. Note that we use LIBXC [13–15] for the PBEsol, revTPSS, Tao–Mo, PKZB, and r<sup>2</sup>SCAN functionals. The dhf-SVP and dhf-TZVP basis sets are employed [16].

	One-Component				Two-Component			
	L–L	$\Gamma$ – $\Gamma$	X–X	L– $\Gamma$	L–L	$\Gamma$ – $\Gamma$	X–X	L– $\Gamma$
dhf-SVP								
S-VWN (III)	3.29	1.88	2.76	0.40	3.04	1.53	2.47	0.33
PBE	3.49	2.16	2.98	0.65	3.25	1.82	2.69	0.64
PBEsol	3.32	2.02	2.89	0.53	3.08	1.67	2.60	0.48
TPSS	3.51	2.37	3.21	0.84	3.27	2.02	2.92	0.82
revTPSS	3.46	2.39	3.24	0.84	3.23	2.05	2.95	0.83
Tao–Mo	3.46	2.51	3.30	0.97	3.23	2.17	3.02	0.98
PKZB	3.60	2.54	3.30	1.01	3.37	2.20	3.01	1.03
r <sup>2</sup> SCAN	4.02	2.83	3.52	1.16	3.79	2.48	3.23	1.28
dhf-TZVP								
S-VWN (III)	3.22	1.86	2.75	0.38	2.96	1.51	2.46	0.30
PBE	3.39	2.14	2.95	0.60	3.15	1.79	2.66	0.60
PBEsol	3.24	2.00	2.87	0.49	2.99	1.65	2.58	0.44
TPSS	3.43	2.34	3.18	0.79	3.18	2.00	2.89	0.78
revTPSS	3.37	2.36	3.20	0.78	3.13	2.01	2.91	0.78
Tao–Mo	3.37	2.47	3.26	0.91	3.13	2.12	2.97	0.92
PKZB	3.50	2.50	3.26	0.95	3.26	2.15	2.97	0.97
r <sup>2</sup> SCAN	3.92	2.80	3.49	1.10	3.68	2.46	3.20	1.23

## II. DENSITY FUNCTIONAL APPROXIMATION STUDY OF SILVER HALIDE CRYSTALS WITH RELAXED STRUCTURES: SCALAR-RELATIVISTIC AND SPIN-ORBIT RESULTS

TABLE IV. Energy band gaps (in eV) and optimized lattice constant  $a$  (in Å) of three-dimensional AgCl (rocksalt structure) for high symmetry points of the FBZ. The local spin density approximation (LSDA) is represented by the S-VWN (III) functional [2, 3], whereas PBE [4] and PBEsol [5] serve as examples for generalized gradient approximations (GGAs). *meta*-GGAs are included through the TPSS [6], revTPSS [7, 8], Tao-Mo [9], PKZB [10], and r<sup>2</sup>SCAN [11, 12] approximations. Note that we use LIBXC [13–15] for the PBEsol, revTPSS, Tao-Mo, PKZB, and r<sup>2</sup>SCAN functionals. The dhf-SVP basis sets is employed [16]. The D3 correction with Becke-Johnson (BJ) damping [17, 18] is applied if stated explicitly. The experimental result for  $a$  is 5.550 Å [19].

Functional	Dispersion	One-Component					Two-Component				
		$a$	L-L	$\Gamma$ - $\Gamma$	X-X	L- $\Gamma$	$a$	L-L	$\Gamma$ - $\Gamma$	X-X	L- $\Gamma$
S-VWN (III)	no D3	5.442	4.08	3.21	3.96	0.59	5.377	3.93	3.27	3.85	0.55
PBE	no D3	5.627	4.64	3.08	4.16	0.92	5.624	4.58	2.91	3.99	0.86
PBEsol	no D3	5.517	4.26	3.14	4.05	0.71	5.515	4.20	2.98	3.89	0.66
TPSS	no D3	5.589	4.61	3.20	4.30	1.02	5.586	4.55	3.04	4.13	0.97
revTPSS	no D3	5.562	4.44	3.18	4.29	0.94	5.561	4.38	3.02	4.13	0.89
Tao-Mo	no D3	5.542	4.29	3.25	4.39	1.02	5.541	4.24	3.10	4.24	0.97
PKZB	no D3	5.640	4.65	3.25	4.41	1.23	5.636	4.59	3.10	4.26	1.18
r <sup>2</sup> SCAN	no D3	5.578	5.07	3.71	4.72	1.47	5.576	5.02	3.55	4.56	1.41
Functional	Dispersion	$a$	L-L	$\Gamma$ - $\Gamma$	X-X	L- $\Gamma$	$a$	L-L	$\Gamma$ - $\Gamma$	X-X	L- $\Gamma$
PBE	D3 BJ	5.556	4.54	3.21	4.18	0.90	5.537	4.47	3.08	4.03	0.85
PBEsol	D3 BJ	5.428	4.12	3.36	4.08	0.71	5.426	4.07	3.20	3.93	0.66
TPSS	D3 BJ	5.500	4.46	3.37	4.33	1.00	5.498	4.40	3.21	4.18	0.94
revTPSS	D3 BJ	5.476	4.29	3.36	4.32	0.93	5.476	4.23	3.20	4.17	0.87
Tao-Mo	D3 BJ	5.513	4.26	3.32	4.40	1.02	5.511	4.20	3.17	4.25	0.97
r <sup>2</sup> SCAN	D3 BJ	5.535	5.02	3.80	4.73	1.47	5.517	4.94	3.68	4.59	1.42

TABLE V. Energy band gaps (in eV) and optimized lattice constant  $a$  (in Å) of three-dimensional AgBr (rocksalt structure) for high symmetry points of the FBZ. The local spin density approximation (LSDA) is represented by the S-VWN (III) functional [2, 3], whereas PBE [4] and PBEsol [5] serve as examples for generalized gradient approximations (GGAs). *meta*-GGAs are included through the TPSS [6], revTPSS [7, 8], Tao–Mo [9], PKZB [10], and r<sup>2</sup>SCAN [11, 12] approximations. Note that we use LIBXC [13–15] for the PBEsol, revTPSS, Tao–Mo, PKZB, and r<sup>2</sup>SCAN functionals. The dhf-SVP basis sets is employed [16]. The D3 correction with Becke–Johnson (BJ) damping [17, 18] is applied if stated explicitly. The experimental result for  $a$  is 5.774 Å[20].

Functional	Dispersion	One-Component					Two-Component				
		$a$	L–L	Γ–Γ	X–X	L–Γ	$a$	L–L	Γ–Γ	X–X	L–Γ
S-VWN (III)	no D3	5.609	3.47	2.82	3.52	0.58	5.604	3.42	2.82	3.39	0.54
PBE	no D3	5.852	4.08	2.63	3.70	0.86	5.849	4.03	2.63	3.54	0.82
PBEsol	no D3	5.695	3.66	2.77	3.59	0.70	5.692	3.60	2.77	3.45	0.65
TPSS	no D3	5.815	4.04	2.90	3.83	1.00	5.812	3.99	2.90	3.68	0.95
revTPSS	no D3	5.789	3.93	2.96	3.81	0.98	5.784	3.87	2.96	3.67	0.94
Tao–Mo	no D3	5.773	3.88	3.07	3.92	1.12	5.738	3.78	3.14	3.79	1.08
PKZB	no D3	5.867	4.17	2.99	3.96	1.24	5.868	4.13	2.99	3.81	1.19
r <sup>2</sup> SCAN	no D3	5.814	4.55	3.36	4.24	1.46	5.811	4.50	3.36	4.09	1.42
Functional	Dispersion	$a$	L–L	Γ–Γ	X–X	L–Γ	$a$	L–L	Γ–Γ	X–X	L–Γ
PBE	D3 BJ	5.750	3.94	2.82	3.72	0.87	5.747	3.89	2.82	3.57	0.83
PBEsol	D3 BJ	5.616	3.53	2.95	3.61	0.72	5.613	3.48	2.95	3.48	0.67
TPSS	D3 BJ	5.710	3.87	3.09	3.85	1.00	5.708	3.82	3.09	3.71	0.95
revTPSS	D3 BJ	5.692	3.77	3.15	3.83	0.99	5.690	3.72	3.14	3.70	0.94
Tao–Mo	D3 BJ	5.745	3.84	3.13	3.93	1.12	5.743	3.79	3.13	3.79	1.08
r <sup>2</sup> SCAN	D3 BJ	5.774	4.50	3.45	4.25	1.47	5.772	4.45	3.44	4.10	1.42



TABLE VI. Energy band gaps (in eV) and optimized lattice constant  $a$  (in Å) of three-dimensional AgI (rocksalt structure) for high symmetry points of the FBZ. The local spin density approximation (LSDA) is represented by the S-VWN (III) functional [2, 3], whereas PBE [4] and PBEsol [5] serve as examples for generalized gradient approximations (GGAs). *meta*-GGAs are included through the TPSS [6], revTPSS [7, 8], Tao–Mo [9], PKZB [10], and r<sup>2</sup>SCAN [11, 12] approximations. Note that we use LIBXC [13–15] for the PBEsol, revTPSS, Tao–Mo, PKZB, and r<sup>2</sup>SCAN functionals. The dhf-SVP basis sets is employed [16]. The D3 correction with Becke–Johnson (BJ) damping [17, 18] is applied if stated explicitly. The experimental result for  $a$  is 6.067 Å[21].

Functional	Dispersion	One-Component					Two-Component				
		$a$	L–L	$\Gamma$ – $\Gamma$	X–X	L– $\Gamma$	$a$	L–L	$\Gamma$ – $\Gamma$	X–X	L– $\Gamma$
S-VWN (III)	no D3	5.938	2.98	2.32	3.00	0.08	5.937	2.73	1.96	2.70	0.46
PBE	no D3	6.189	3.52	2.13	2.96	0.68	6.187	3.27	1.79	2.67	0.64
PBEsol	no D3	6.025	3.13	2.28	3.03	0.33	6.023	2.88	1.93	2.74	0.54
TPSS	no D3	6.156	3.49	2.39	3.22	0.82	6.153	3.25	2.05	2.94	0.83
revTPSS	no D3	6.118	3.39	2.48	3.28	0.77	6.116	3.15	2.13	3.00	0.85
Tao–Mo	no D3	6.097	3.36	2.64	3.37	0.88	6.071	3.10	2.34	3.11	1.04
PKZB	no D3	6.203	3.65	2.49	3.27	1.06	6.200	3.41	2.15	2.99	1.02
r <sup>2</sup> SCAN	no D3	6.161	4.01	2.84	3.52	1.15	6.159	3.78	2.50	3.24	1.29
Functional	Dispersion	$a$	L–L	$\Gamma$ – $\Gamma$	X–X	L– $\Gamma$	$a$	L–L	$\Gamma$ – $\Gamma$	X–X	L– $\Gamma$
PBE	D3 BJ	6.078	3.369	2.32	3.06	0.53	6.067	3.11	1.99	2.78	0.69
PBEsol	D3 BJ	5.930	2.986	2.48	3.13	0.19	5.927	2.74	2.12	2.84	0.61
TPSS	D3 BJ	5.983	3.227	2.71	3.37	0.58	5.982	2.99	2.35	3.10	0.91
revTPSS	D3 BJ	5.955	3.130	2.79	3.35	0.53	5.949	2.88	2.44	3.16	0.94
Tao–Mo	D3 BJ	6.078	3.339	2.67	3.39	0.85	6.068	3.10	2.35	3.11	1.04
r <sup>2</sup> SCAN	D3 BJ	6.159	4.011	2.84	3.53	1.14	6.156	3.77	2.51	3.24	1.29

### III. FURTHER RESULTS FOR THE INDIUM(I,III)-TELLURIDE TWO-DIMENSIONAL HONEYCOMB SYSTEM

The unit cell parameters and electronic band structures are calculated without the D3-BJ correction for comparison to the results in the main text. Additionally, the cell structure was optimized without taking spin-orbit coupling into account [22, 23]. All other computational parameters are unchanged compared to the study in the main text. In detail, we use the PBE functional [4] combined with the dhf-TZVP-2c basis sets [16]. A  $k$  mesh of  $32 \times 32$  is employed. A Gaussian smearing of 0.001 Hartree [24] and an SCF threshold of  $10^{-8}$  Hartree are chosen. The electronic band structure is displayed in Figure 1.

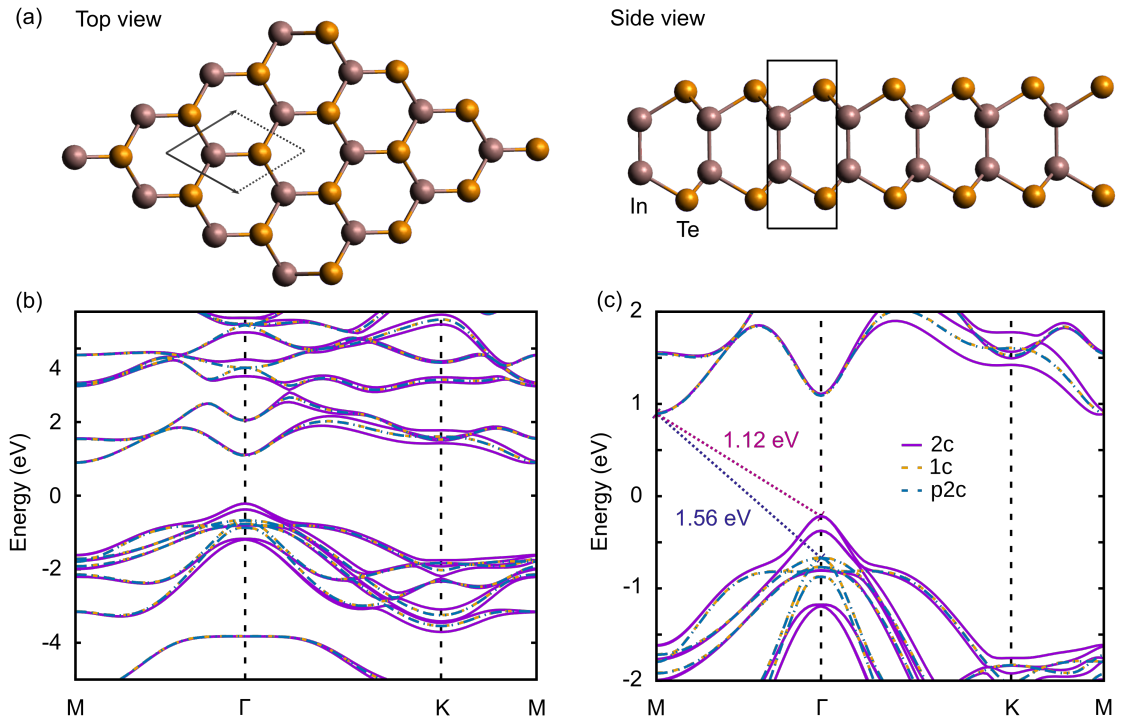


FIG. 1. (a) Top and side views of the two-dimensional InTe honeycomb system, with indicated unit cell. The unit cell consists of two In and two Te atoms, marked with vertical black lines. (b,c) Electronic band structure of the FBZ. The orange dashed lines are calculated without spin-orbit coupling in a one-component (1c) formalism, while the solid purple lines include spin-orbit interactions in the two-component (2c) methodology. The powder blue lines mark the two-component calculations with spin-orbit ECPs scaled to zero, i.e. the pseudo two-component (p2c) version. The black vertical dashed lines mark the  $\Gamma$  and K points of the Brillouin zone. Band gaps are indicated in blue (1c) and purple (2c) in panel (c).

## IV. STRUCTURES

Structures are given in TURBOMOLE format [25–27]. Cell parameters (`$cell`) are given in atomic units unless stated differently, i.e. `angs` for Ångström. Coordinates in the cell (`$coord`) are always given in atomic units.

### A. Computation Times

```
$cell
6.61460836 6.61460836 6.61460836 60.0 60.0 60.0
$coord
0.0000000000000000 0.0000000000000000 0.0000000000000000 pb
$end
```

## B. Ionization Potentials of Heavy *p*-Elements

```
$coord
  0.0000000000000000  0.0000000000000000  0.0000000000000000  in
$end

$coord
  0.0000000000000000  0.0000000000000000  0.0000000000000000  sn
$end

$coord
  0.0000000000000000  0.0000000000000000  0.0000000000000000  sb
$end

$coord
  0.0000000000000000  0.0000000000000000  0.0000000000000000  te
$end

$coord
  0.0000000000000000  0.0000000000000000  0.0000000000000000  i
$end

$coord
  0.0000000000000000  0.0000000000000000  0.0000000000000000  tl
$end

$coord
  0.0000000000000000  0.0000000000000000  0.0000000000000000  pb
$end

$coord
  0.0000000000000000  0.0000000000000000  0.0000000000000000  bi
$end

$coord
  0.0000000000000000  0.0000000000000000  0.0000000000000000  po
$end

$coord
  0.0000000000000000  0.0000000000000000  0.0000000000000000  at
$end
```

## C. Band Structures of Three-Dimensional Gold and Lead Crystals

a) Three-dimensional gold fcc crystal

\$cell

5.45185 5.45185 5.45185 60.0 60.0 60.0

\$coord

0.0000000000000000 0.0000000000000000 0.0000000000000000 au

\$end

b) Three-dimensional lead fcc crystal

\$cell

6.57429 6.57429 6.57429 60.0 60.0 60.0

\$coord

0.0000000000000000 0.0000000000000000 0.0000000000000000 pb

\$end

## D. Band Gaps of Three-Dimensional Silver Halide Crystals

a) Non-relaxed structures

i) AgCl

```
$cell ang  
3.9683 3.9683 3.9683 60.0000 60.0000 60.0000  
$coord frac  
0.0000000000000000 0.0000000000000000 0.0000000000000000 ag  
0.5000000000000000 0.5000000000000000 0.5000000000000000 cl  
$end
```

ii) AgBr

```
$cell ang  
4.1316 4.1316 4.1316 60.0000 60.0000 60.0000  
$coord frac  
0.0000000000000000 0.0000000000000000 0.0000000000000000 ag  
0.5000000000000000 0.5000000000000000 0.5000000000000000 br  
$end
```

iii) AgI

```
$cell ang  
4.3621 4.3621 4.3621 60.0000 60.0000 60.0000  
$coord frac  
0.0000000000000000 0.0000000000000000 0.0000000000000000 ag  
0.5000000000000000 0.5000000000000000 0.5000000000000000 i  
$end
```

b) Relaxed structures without D3-BJ

i) AgCl

SVWN

\$cell ang

3.8482534450333333333 3.8482534450333333333 3.8482534450333333333 60.0 60.0 60.0

\$coord frac

0.000000000000000 0.000000000000000 0.000000000000000 ag

0.500000000000000 0.500000000000000 0.500000000000000 c1

\$end

PBE

\$cell ang

3.9788179075666666666 3.9788179075666666666 3.9788179075666666666 60.0 60.0 60.0

\$coord frac

0.000000000000000 0.000000000000000 0.000000000000000 ag

0.500000000000000 0.500000000000000 0.500000000000000 c1

\$end

PBEsol

\$cell ang

3.9008004988333333333 3.9008004988333333333 3.9008004988333333333 60.0 60.0 60.0

\$coord frac

0.000000000000000 0.000000000000000 0.000000000000000 ag

0.500000000000000 0.500000000000000 0.500000000000000 c1

\$end

TPSS

\$cell ang

3.9519279141000000000 3.9519279141000000000 3.9519279141000000000 60.0 60.0 60.0

\$coord frac

0.000000000000000 0.000000000000000 0.000000000000000 ag

0.500000000000000 0.500000000000000 0.500000000000000 c1

\$end

revTPSS

\$cell ang

3.93323644336667 3.93323644336667 3.93323644336667 60.0 60.0 60.0

\$coord frac

0.000000000000000 0.000000000000000 0.000000000000000 ag

0.500000000000000 0.500000000000000 0.500000000000000 c1

\$end

Tao-Mo

\$cell ang

3.9184690781 3.9184690781 3.9184690781 60.0 60.0 60.0

\$coord frac

0.000000000000000 0.000000000000000 0.000000000000000 ag  
0.500000000000000 0.500000000000000 0.500000000000000 c1

\$end

PKZB

\$cell ang

3.9880650068 3.9880650068 3.9880650068 60.0 60.0 60.0

\$coord frac

0.000000000000000 0.000000000000000 0.000000000000000 ag  
0.500000000000000 0.500000000000000 0.500000000000000 c1

\$end

r2SCAN

\$cell ang

3.94398068143333333333 3.94398068143333333333 3.94398068143333333333 60.0 60.0 60.0

\$coord frac

0.000000000000000 0.000000000000000 0.000000000000000 ag  
0.500000000000000 0.500000000000000 0.500000000000000 c1

\$end

2c-SVWN

\$cell ang

3.8017642716 3.8017642716 3.8017642716 60.0 60.0 60.0

\$coord frac

0.000000000000000 0.000000000000000 0.000000000000000 ag  
0.500000000000000 0.500000000000000 0.500000000000000 c1

\$end

2c-PBE

\$cell ang

3.97687054476666666666 3.97687054476666666666 3.97687054476666666666 60.0 60.0 60.0

\$coord frac

0.000000000000000 0.000000000000000 0.000000000000000 ag  
0.500000000000000 0.500000000000000 0.500000000000000 c1

\$end

2c-PBEsol

\$cell ang

3.89940465353333333333 3.89940465353333333333 3.89940465353333333333 60.0 60.0 60.0

\$coord frac

0.000000000000000 0.000000000000000 0.000000000000000 ag  
0.500000000000000 0.500000000000000 0.500000000000000 c1

\$end



2c-TPSS

\$cell ang

3.950071428333333333 3.950071428333333333 3.950071428333333333 60.0 60.0 60.0

\$coord frac

0.000000000000000 0.000000000000000 0.000000000000000 ag  
0.500000000000000 0.500000000000000 0.500000000000000 c1

\$end

2c-revTPSS

\$cell ang

3.932278996066666666 3.932278996066666666 3.932278996066666666 60.0 60.0 60.0

\$coord frac

0.000000000000000 0.000000000000000 0.000000000000000 ag  
0.500000000000000 0.500000000000000 0.500000000000000 c1

\$end

2c-Tao-Mo

\$cell ang

3.918427878766666666 3.918427878766666666 3.918427878766666666 60.0 60.0 60.0

\$coord frac

0.000000000000000 0.000000000000000 0.000000000000000 ag  
0.500000000000000 0.500000000000000 0.500000000000000 c1

\$end

2c-PKZB

\$cell ang

3.9852599056 3.9852599056 3.9852599056 60.0 60.0 60.0

\$coord frac

0.000000000000000 0.000000000000000 0.000000000000000 ag  
0.500000000000000 0.500000000000000 0.500000000000000 c1

\$end

2c-r2SCAN

\$cell ang

3.9430444896 3.9430444896 3.9430444896 60.0 60.0 60.0

\$coord frac

0.000000000000000 0.000000000000000 0.000000000000000 ag  
0.500000000000000 0.500000000000000 0.500000000000000 c1

\$end

ii) AgBr

SVWN

\$cell angs

3.9659229888 3.9659229888 3.9659229888 60.0 60.0 60.0

\$coord frac

0.000000000000000 0.000000000000000 0.000000000000000 ag

0.500000000000000 0.500000000000000 0.500000000000000 br

\$end

PBE

\$cell angs

4.13768026056666666666 4.13768026056666666666 4.13768026056666666666 60.0 60.0 60.0

\$coord frac

0.000000000000000 0.000000000000000 0.000000000000000 ag

0.500000000000000 0.500000000000000 0.500000000000000 br

\$end

PBEsol

\$cell angs

4.02721811653333333333 4.02721811653333333333 4.02721811653333333333 60.0 60.0 60.0

\$coord frac

0.000000000000000 0.000000000000000 0.000000000000000 ag

0.500000000000000 0.500000000000000 0.500000000000000 br

\$end

TPSS

\$cell angs

4.11184283506666666666 4.11184283506666666666 4.11184283506666666666 60.0 60.0 60.0

\$coord frac

0.000000000000000 0.000000000000000 0.000000000000000 ag

0.500000000000000 0.500000000000000 0.500000000000000 br

\$end

revTPSS

\$cell angs

4.09371116283333333333 4.09371116283333333333 4.09371116283333333333 60.0 60.0 60.0

\$coord frac

0.000000000000000 0.000000000000000 0.000000000000000 ag

0.500000000000000 0.500000000000000 0.500000000000000 br

\$end

Tao-Mo

\$cell angs

4.0823834939333333333 4.0823834939333333333 4.0823834939333333333 60.0 60.0 60.0

\$coord frac

0.000000000000000 0.000000000000000 0.000000000000000 ag  
0.500000000000000 0.500000000000000 0.500000000000000 br

\$end

PKZB

\$cell angs

4.1489044119666666666 4.1489044119666666666 4.1489044119666666666 60.0 60.0 60.0

\$coord frac

0.000000000000000 0.000000000000000 0.000000000000000 ag  
0.500000000000000 0.500000000000000 0.500000000000000 br

\$end

r2SCAN

\$cell angs

4.1107789573333333333 4.1107789573333333333 4.1107789573333333333 60.0 60.0 60.0

\$coord frac

0.000000000000000 0.000000000000000 0.000000000000000 ag  
0.500000000000000 0.500000000000000 0.500000000000000 br

\$end

2c-SVWN

\$cell angs

3.9626048018 3.9626048018 3.9626048018 60.0 60.0 60.0

\$coord frac

0.000000000000000 0.000000000000000 0.000000000000000 ag  
0.500000000000000 0.500000000000000 0.500000000000000 br

\$end

2c-PBE

\$cell angs

4.1361743430333333333 4.1361743430333333333 4.1361743430333333333 60.0 60.0 60.0

\$coord frac

0.000000000000000 0.000000000000000 0.000000000000000 ag  
0.500000000000000 0.500000000000000 0.500000000000000 br

\$end

2c-PBEsol

\$cell angs

4.0248079197666666666 4.0248079197666666666 4.0248079197666666666 60.0 60.0 60.0

\$coord frac

0.000000000000000 0.000000000000000 0.000000000000000 ag  
0.500000000000000 0.500000000000000 0.500000000000000 br

\$end

2c-TPSS

\$cell ang

4.11004402016666666666 4.11004402016666666666 4.11004402016666666666 60.0 60.0 60.0

\$coord frac

0.0000000000000000 0.0000000000000000 0.0000000000000000 ag

0.5000000000000000 0.5000000000000000 0.5000000000000000 br

\$end

2c-revTPSS

\$cell ang

4.0897251878 4.0897251878 4.0897251878 60.0 60.0 60.0

\$coord frac

0.0000000000000000 0.0000000000000000 0.0000000000000000 ag

0.5000000000000000 0.5000000000000000 0.5000000000000000 br

\$end

2c-Tao-Mo

\$cell ang

4.05717500276666666666 4.05717500276666666666 4.05717500276666666666 60.0 60.0 60.0

\$coord frac

0.0000000000000000 0.0000000000000000 0.0000000000000000 ag

0.5000000000000000 0.5000000000000000 0.5000000000000000 br

\$end

2c-PKZB

\$cell ang

4.14933946790000000000 4.14933946790000000000 4.14933946790000000000 60.0 60.0 60.0

\$coord frac

0.0000000000000000 0.0000000000000000 0.0000000000000000 ag

0.5000000000000000 0.5000000000000000 0.5000000000000000 br

\$end

2c-r2SCAN

\$cell ang

4.10922457123333333333 4.10922457123333333333 4.10922457123333333333 60.0 60.0 60.0

\$coord frac

0.0000000000000000 0.0000000000000000 0.0000000000000000 ag

0.5000000000000000 0.5000000000000000 0.5000000000000000 br

\$end

iii) AgI

SVWN

\$cell angstroms

4.19916806426666666666 4.19916806426666666666 4.19916806426666666666 60.0 60.0 60.0

\$coord fraction

0.0000000000000000 0.0000000000000000 0.0000000000000000 ag

0.5000000000000000 0.5000000000000000 0.5000000000000000 i

\$end

PBE

\$cell angstroms

4.375962455 4.375962455 4.375962455 60.0 60.0 60.0

\$coord fraction

0.0000000000000000 0.0000000000000000 0.0000000000000000 ag

0.5000000000000000 0.5000000000000000 0.5000000000000000 i

\$end

PBEsol

\$cell angstroms

4.2604273368 4.2604273368 4.2604273368 60.0 60.0 60.0

\$coord fraction

0.0000000000000000 0.0000000000000000 0.0000000000000000 ag

0.5000000000000000 0.5000000000000000 0.5000000000000000 i

\$end

TPSS

\$cell angstroms

4.35287278606666666666 4.35287278606666666666 4.35287278606666666666 60.0 60.0 60.0

\$coord fraction

0.0000000000000000 0.0000000000000000 0.0000000000000000 ag

0.5000000000000000 0.5000000000000000 0.5000000000000000 i

\$end

revTPSS

\$cell angstroms

4.326282372 4.326282372 4.326282372 60.0 60.0 60.0

\$coord fraction

0.0000000000000000 0.0000000000000000 0.0000000000000000 ag

0.5000000000000000 0.5000000000000000 0.5000000000000000 i

\$end

Tao-Mo

\$cell angs

4.31120483906666666666 4.31120483906666666666 4.31120483906666666666 60.0 60.0 60.0

\$coord frac

0.000000000000000 0.000000000000000 0.000000000000000 ag  
0.500000000000000 0.500000000000000 0.500000000000000 i

\$end

PKZB

\$cell angs

4.38623378086666666666 4.38623378086666666666 4.38623378086666666666 60.0 60.0 60.0

\$coord frac

0.000000000000000 0.000000000000000 0.000000000000000 ag  
0.500000000000000 0.500000000000000 0.500000000000000 i

\$end

r2SCAN

\$cell angs

4.35615418616666666666 4.35615418616666666666 4.35615418616666666666 60.0 60.0 60.0

\$coord frac

0.000000000000000 0.000000000000000 0.000000000000000 ag  
0.500000000000000 0.500000000000000 0.500000000000000 i

\$end

2c-SVWN

\$cell angs

4.19790823766666666666 4.19790823766666666666 4.19790823766666666666 60.0 60.0 60.0

\$coord frac

0.000000000000000 0.000000000000000 0.000000000000000 ag  
0.500000000000000 0.500000000000000 0.500000000000000 i

\$end

2c-PBE

\$cell angs

4.374539102 4.374539102 4.374539102 60.0 60.0 60.0

\$coord frac

0.000000000000000 0.000000000000000 0.000000000000000 ag  
0.500000000000000 0.500000000000000 0.500000000000000 i

\$end

2c-PBEsol

\$cell angs

4.25857171496666666666 4.25857171496666666666 4.25857171496666666666 60.0 60.0 60.0

\$coord frac

0.000000000000000 0.000000000000000 0.000000000000000 ag  
0.500000000000000 0.500000000000000 0.500000000000000 i

\$end

2c-TPSS

\$cell ang

4.35102446196666666666 4.35102446196666666666 4.35102446196666666666 60.0 60.0 60.0

\$coord frac

0.000000000000000 0.000000000000000 0.000000000000000 ag  
0.500000000000000 0.500000000000000 0.500000000000000 i

\$end

2c-revTPSS

\$cell ang

4.32457321323333333333 4.32457321323333333333 4.32457321323333333333 60.0 60.0 60.0

\$coord frac

0.000000000000000 0.000000000000000 0.000000000000000 ag  
0.500000000000000 0.500000000000000 0.500000000000000 i

\$end

2c-Tao-Mo

\$cell ang

4.2926534394 4.2926534394 4.2926534394 60.0 60.0 60.0

\$coord frac

0.000000000000000 0.000000000000000 0.000000000000000 ag  
0.500000000000000 0.500000000000000 0.500000000000000 i

\$end

2c-PKZB

\$cell ang

4.38391013183333333333 4.38391013183333333333 4.38391013183333333333 60.0 60.0 60.0

\$coord frac

0.000000000000000 0.000000000000000 0.000000000000000 ag  
0.500000000000000 0.500000000000000 0.500000000000000 i

\$end

2c-r2SCAN

\$cell ang

4.35527771656666666666 4.35527771656666666666 4.35527771656666666666 60.0 60.0 60.0

\$coord frac

0.000000000000000 0.000000000000000 0.000000000000000 ag  
0.500000000000000 0.500000000000000 0.500000000000000 i

\$end

c) Relaxed structures with D3-BJ

i) AgCl

PBE-D3-BJ

\$cell ang

3.92879622146666666666 3.92879622146666666666 3.92879622146666666666 60.0 60.0 60.0

\$coord frac

0.00325673735477 0.00601902380048 0.00412222047542 ag

0.50331882947054 0.50572722588679 0.50448910771799 cl

\$end

PBEsol-D3-BJ

\$cell ang

3.83841735613333333333 3.83841735613333333333 3.83841735613333333333 60.0 60.0 60.0

\$coord frac

0.00325673735477 0.00601902380048 0.00412222047542 ag

0.50331882947054 0.50572722588679 0.50448910771799 cl

\$end

TPSS-D3-BJ

\$cell ang

3.88912460836666666666 3.88912460836666666666 3.88912460836666666666 60.0 60.0 60.0

\$coord frac

0.00325673735477 0.00601902380048 0.00412222047542 ag

0.50331882947054 0.50572722588679 0.50448910771799 cl

\$end

revTPSS-D3-BJ

\$cell ang

3.87246070486666666666 3.87246070486666666666 3.87246070486666666666 60.0 60.0 60.0

\$coord frac

0.00325673735477 0.00601902380048 0.00412222047542 ag

0.50331882947054 0.50572722588679 0.50448910771799 cl

\$end

Tao-Mo-D3-BJ

\$cell ang

3.8983235666 3.8983235666 3.8983235666 60.0 60.0 60.0

\$coord frac

0.00325673735477 0.00601902380048 0.00412222047542 ag

0.50331882947054 0.50572722588679 0.50448910771799 cl

\$end



r2SCAN-D3-BJ

\$cell angs

3.913670709 3.913670709 3.913670709 60.0 60.0 60.0

\$coord frac

0.00325673735477 0.00601902380048 0.00412222047542 ag  
0.50331882947054 0.50572722588679 0.50448910771799 cl

\$end

2c-PBE-D3-BJ

\$cell angs

3.91521636993333333333 3.91521636993333333333 3.91521636993333333333 60.0 60.0 60.0

\$coord frac

0.00325673735477 0.00601902380048 0.00412222047542 ag  
0.50331882947054 0.50572722588679 0.50448910771799 cl

\$end

2c-PBEsol-D3-BJ

\$cell angs

3.83689838036666666666 3.83689838036666666666 3.83689838036666666666 60.0 60.0 60.0

\$coord frac

0.0000000000000000 0.0000000000000000 0.0000000000000000 ag  
0.5000000000000000 0.5000000000000000 0.5000000000000000 cl

\$end

2c-TPSS-D3-BJ

\$cell angs

3.8874918142 3.8874918142 3.8874918142 60.0 60.0 60.0

\$coord frac

0.00325673735477 0.00601902380048 0.00412222047542 ag  
0.50331882947054 0.50572722588679 0.50448910771799 cl

\$end

2c-revTPSS-D3-BJ

\$cell angs

3.8711454888 3.8711454888 3.8711454888 60.0 60.0 60.0

\$coord frac

0.00325673735477 0.00601902380048 0.00412222047542 ag  
0.50331882947054 0.50572722588679 0.50448910771799 cl

\$end

2c-Tao-Mo-D3-BJ

\$cell angs

3.8970339839 3.8970339839 3.8970339839 60.0 60.0 60.0

\$coord frac

0.00325673735477 0.00601902380048 0.00412222047542 ag  
0.50331882947054 0.50572722588679 0.50448910771799 cl

\$end

2c-r2SCAN-D3-BJ

\$cell angs

3.90136349976666666666 3.90136349976666666666 3.90136349976666666666 60.0 60.0 60.0

\$coord frac

0.00833854180292 0.00573591628562 0.00017944551823 ag

0.50829278335618 0.50568083319942 0.50013567738648 cl

\$end

ii) AgBr

PBE-D3-BJ

\$cell angs

4.0656560669 4.0656560669 4.0656560669 60.0 60.0 60.0

\$coord frac

0.000000000000000 0.000000000000000 0.000000000000000 ag

0.500000000000000 0.500000000000000 0.500000000000000 br

\$end

PBEsol-D3-BJ

\$cell angs

3.9711451685 3.9711451685 3.9711451685 60.0 60.0 60.0

\$coord frac

0.000000000000000 0.000000000000000 0.000000000000000 ag

0.500000000000000 0.500000000000000 0.500000000000000 br

\$end

TPSS-D3-BJ

\$cell angs

4.0377456864 4.0377456864 4.0377456864 60.0 60.0 60.0

\$coord frac

0.000000000000000 0.000000000000000 0.000000000000000 ag

0.500000000000000 0.500000000000000 0.500000000000000 br

\$end

revTPSS-D3-BJ

\$cell angs

4.02469085823333333333 4.02469085823333333333 4.02469085823333333333 60.0 60.0 60.0

\$coord frac

0.000000000000000 0.000000000000000 0.000000000000000 ag

0.500000000000000 0.500000000000000 0.500000000000000 br

\$end

Tao-Mo-D3-BJ

\$cell angs

4.06252851366666666666 4.06252851366666666666 4.06252851366666666666 60.0 60.0 60.0

\$coord frac

0.000000000000000 0.000000000000000 0.000000000000000 ag

0.500000000000000 0.500000000000000 0.500000000000000 br

\$end

r2SCAN-D3-BJ

\$cell angs

4.082712298 4.082712298 4.082712298 60.0 60.0 60.0

\$coord frac

0.00000000000000 0.00000000000000 0.00000000000000 ag  
0.50000000000000 0.50000000000000 0.50000000000000 br

\$end

2c-PBE-D3-BJ

\$cell angs

4.06356866316666666666 4.06356866316666666666 4.06356866316666666666 60.0 60.0 60.0

\$coord frac

0.00000000000000 0.00000000000000 0.00000000000000 ag  
0.50000000000000 0.50000000000000 0.50000000000000 br

\$end

2c-PBEsol-D3-BJ

\$cell angs

3.96911415466666666666 3.96911415466666666666 3.96911415466666666666 60.0 60.0 60.0

\$coord frac

0.00000000000000 0.00000000000000 0.00000000000000 ag  
0.50000000000000 0.50000000000000 0.50000000000000 br

\$end

2c-TPSS-D3-BJ

\$cell angs

4.03638224546666666666 4.03638224546666666666 4.03638224546666666666 60.0 60.0 60.0

\$coord frac

0.00000000000000 0.00000000000000 0.00000000000000 ag  
0.50000000000000 0.50000000000000 0.50000000000000 br

\$end

2c-revTPSS-D3-BJ

\$cell angs

4.0234614894 4.0234614894 4.0234614894 60.0 60.0 60.0

\$coord frac

0.00000000000000 0.00000000000000 0.00000000000000 ag  
0.50000000000000 0.50000000000000 0.50000000000000 br

\$end

2c-Tao-Mo-D3-BJ

\$cell angs

4.0611942705 4.0611942705 4.0611942705 60.0 60.0 60.0

\$coord frac

0.00000000000000 0.00000000000000 0.00000000000000 ag  
0.50000000000000 0.50000000000000 0.50000000000000 br

\$end

2c-r2SCAN-D3-BJ

\$cell angs

4.0811353733 4.0811353733 4.0811353733 60.0 60.0 60.0

\$coord frac

0.0000000000000000 0.0000000000000000 0.0000000000000000 ag

0.5000000000000000 0.5000000000000000 0.5000000000000000 br

\$end

iii) AgI

PBE-D3-BJ

\$cell ang

4.2976226375333333333 4.2976226375333333333 4.2976226375333333333 60.0 60.0 60.0

\$coord frac

0.000000000000000 0.000000000000000 0.000000000000000 ag

0.500000000000000 0.500000000000000 0.500000000000000 i

\$end

PBEsol-D3-BJ

\$cell ang

4.1928343046666666666 4.1928343046666666666 4.1928343046666666666 60.0 60.0 60.0

\$coord frac

0.000000000000000 0.000000000000000 0.000000000000000 ag

0.500000000000000 0.500000000000000 0.500000000000000 i

\$end

TPSS-D3-BJ

\$cell ang

4.2305662249666666666 4.2305662249666666666 4.2305662249666666666 60.0 60.0 60.0

\$coord frac

0.000000000000000 0.000000000000000 0.000000000000000 ag

0.500000000000000 0.500000000000000 0.500000000000000 i

\$end

revTPSS-D3-BJ

\$cell ang

4.2109555586 4.2109555586 4.2109555586 60.0 60.0 60.0

\$coord frac

0.000000000000000 0.000000000000000 0.000000000000000 ag

0.500000000000000 0.500000000000000 0.500000000000000 i

\$end

Tao-Mo-D3-BJ

\$cell ang

4.2978985725666666666 4.2978985725666666666 4.2978985725666666666 60.0 60.0 60.0

\$coord frac

0.000000000000000 0.000000000000000 0.000000000000000 ag

0.500000000000000 0.500000000000000 0.500000000000000 i

\$end

r2SCAN-D3-BJ

\$cell ang

4.3548993639 4.3548993639 4.3548993639 60.0 60.0 60.0

\$coord frac

0.0000000000000000 0.0000000000000000 0.0000000000000000 ag  
0.5000000000000000 0.5000000000000000 0.5000000000000000 i

\$end

2c-PBE-D3-BJ

\$cell ang

4.2899779228 4.2899779228 4.2899779228 60.0 60.0 60.0

\$coord frac

0.0000000000000000 0.0000000000000000 0.0000000000000000 ag  
0.5000000000000000 0.5000000000000000 0.5000000000000000 i

\$end

2c-PBEsol-D3-BJ

\$cell ang

4.19121877706666666666 4.19121877706666666666 4.19121877706666666666 60.0 60.0 60.0

\$coord frac

0.0000000000000000 0.0000000000000000 0.0000000000000000 ag  
0.5000000000000000 0.5000000000000000 0.5000000000000000 i

\$end

2c-TPSS-D3-BJ

\$cell ang

4.22982934023333333333 4.22982934023333333333 4.22982934023333333333 60.0 60.0 60.0

\$coord frac

0.0000000000000000 0.0000000000000000 0.0000000000000000 ag  
0.5000000000000000 0.5000000000000000 0.5000000000000000 i

\$end

2c-revTPSS-D3-BJ

\$cell ang

4.20627833826666666666 4.20627833826666666666 4.20627833826666666666 60.0 60.0 60.0

\$coord frac

0.0000000000000000 0.0000000000000000 0.0000000000000000 ag  
0.5000000000000000 0.5000000000000000 0.5000000000000000 i

\$end

2c-Tao-Mo-D3-BJ

\$cell ang

4.29099278693333333333 4.29099278693333333333 4.29099278693333333333 60.0 60.0 60.0

\$coord frac

0.0000000000000000 0.0000000000000000 0.0000000000000000 ag  
0.5000000000000000 0.5000000000000000 0.5000000000000000 i

\$end

2c-r2SCAN-D3-BJ

\$cell angs

4.3530927047 4.3530927047 4.3530927047 60.0 60.0 60.0

\$coord frac

0.0000000000000000 0.0000000000000000 0.0000000000000000 ag

0.5000000000000000 0.5000000000000000 0.5000000000000000 i

\$end



## E. Indium(I,III)-Telluride Two-Dimensional Honeycomb Structure

a) 1c optimization without D3

\$cell

8.0124390 8.0124390 60.0

\$coord

0.000000000000000	0.000000000000000	0.000000000000000	in
0.00125810178926	0.00074629401429	5.30945552703617	in
4.00628439107714	2.31300606929462	-2.75618224113402	te
4.00743098931212	2.31368907685671	8.06634157724272	te

\$end

b) 1c optimization with D3

\$cell

8.1284346 8.1284346 60.0

\$coord

0.000000000000000	0.000000000000000	0.000000000000000	in
-0.06652862961313	-0.03162410986896	5.26037245584803	in
4.05404267216884	2.34660351650535	-2.66669727508479	te
3.99957189577787	2.31977601108490	7.92597890841854	te

\$end

c) 2c optimization with D3

\$cell

8.1284346 8.1284346 60.0

\$coord

0.000000000000000	0.000000000000000	0.000000000000000	in
0.000000000000000	0.000000000000000	5.26273509093640	in
4.05997252052396	2.34549030506129	-2.67054225966576	te
4.05997252052396	2.34549030506129	7.93471996528309	te

\$end

## F. One-Dimensional Platinum Chains

\$cell ang

4.0

\$coord

0.00000000000000 0.00000000000000 0.00000000000000 pt

3.77945197720000 0.00000000000000 0.00000000000000 pt

\$end

\$cell ang

4.1

\$coord

0.00000000000000 0.00000000000000 0.00000000000000 pt

3.87393827660000 0.00000000000000 0.00000000000000 pt

\$end

\$cell ang

4.2

\$coord

0.00000000000000 0.00000000000000 0.00000000000000 pt

3.96842457600000 0.00000000000000 0.00000000000000 pt

\$end

\$cell ang

4.3

\$coord

0.00000000000000 0.00000000000000 0.00000000000000 pt

4.06291087540000 0.00000000000000 0.00000000000000 pt

\$end

\$cell ang

4.4

\$coord

0.00000000000000 0.00000000000000 0.00000000000000 pt

4.15739717490000 0.00000000000000 0.00000000000000 pt

\$end

\$cell ang

4.5

\$coord

0.00000000000000 0.00000000000000 0.00000000000000 pt

4.25188347430000 0.00000000000000 0.00000000000000 pt

\$end

```

$cell_angs
4.6
$coord
    0.0000000000000000    0.0000000000000000    0.0000000000000000    pt
    4.34636977370000    0.0000000000000000    0.0000000000000000    pt
$end

```

```

$cell_angs
4.7
$coord
    0.0000000000000000    0.0000000000000000    0.0000000000000000    pt
    4.44085607320000    0.0000000000000000    0.0000000000000000    pt
$end

```

```

$cell_angs
4.8
$coord
    0.0000000000000000    0.0000000000000000    0.0000000000000000    pt
    4.53534237260000    0.0000000000000000    0.0000000000000000    pt
$end

```

```

$cell_angs
4.9
$coord
    0.0000000000000000    0.0000000000000000    0.0000000000000000    pt
    4.62982867200000    0.0000000000000000    0.0000000000000000    pt
$end

```

```

$cell_angs
5.0
$coord
    0.0000000000000000    0.0000000000000000    0.0000000000000000    pt
    4.72431497140000    0.0000000000000000    0.0000000000000000    pt
$end

```

```

$cell_angs
5.1
$coord
    0.0000000000000000    0.0000000000000000    0.0000000000000000    pt
    4.81880127090000    0.0000000000000000    0.0000000000000000    pt
$end

```

```

$cell_angs
5.11
$coord
    0.0000000000000000    0.0000000000000000    0.0000000000000000    pt
    4.8282500000000000    0.0000000000000000    0.0000000000000000    pt
$end

```

```

$cell_angs
5.12
$coord
  0.000000000000000  0.000000000000000  0.000000000000000  pt
  4.837699000000000  0.000000000000000  0.000000000000000  pt
$end

```

```

$cell_angs
5.15
$coord
  0.000000000000000  0.000000000000000  0.000000000000000  pt
  4.866045000000000  0.000000000000000  0.000000000000000  pt
$end

```

```

$cell_angs
5.2
$coord
  0.000000000000000  0.000000000000000  0.000000000000000  pt
  4.913287570300000  0.000000000000000  0.000000000000000  pt
$end

```

```

$cell_angs
5.25
$coord
  0.000000000000000  0.000000000000000  0.000000000000000  pt
  4.960531000000000  0.000000000000000  0.000000000000000  pt
$end

```

```

$cell_angs
5.3
$coord
  0.000000000000000  0.000000000000000  0.000000000000000  pt
  5.007773869700000  0.000000000000000  0.000000000000000  pt
$end

```

```

$cell_angs
5.35
$coord
  0.000000000000000  0.000000000000000  0.000000000000000  pt
  5.055015000000000  0.000000000000000  0.000000000000000  pt
$end

```

```

$cell_angs
5.4
$coord
    0.0000000000000000    0.0000000000000000    0.0000000000000000    pt
    5.10226016920000    0.0000000000000000    0.0000000000000000    pt
$end

```

```

$cell_angs
5.5
$coord
    0.0000000000000000    0.0000000000000000    0.0000000000000000    pt
    5.19674646860000    0.0000000000000000    0.0000000000000000    pt
$end

```

```

$cell_angs
5.6
$coord
    0.0000000000000000    0.0000000000000000    0.0000000000000000    pt
    5.29123276800000    0.0000000000000000    0.0000000000000000    pt
$end

```

```

$cell_angs
5.7
$coord
    0.0000000000000000    0.0000000000000000    0.0000000000000000    pt
    5.38571906740000    0.0000000000000000    0.0000000000000000    pt
$end

```

```

$cell_angs
5.8
$coord
    0.0000000000000000    0.0000000000000000    0.0000000000000000    pt
    5.48020536690000    0.0000000000000000    0.0000000000000000    pt
$end

```

```

$cell_angs
5.9
$coord
    0.0000000000000000    0.0000000000000000    0.0000000000000000    pt
    5.57469166630000    0.0000000000000000    0.0000000000000000    pt
$end

```

```

$cell_angs
6.0
$coord
    0.0000000000000000    0.0000000000000000    0.0000000000000000    pt
    5.66917796570000    0.0000000000000000    0.0000000000000000    pt
$end

```

- 
- [1] R. Zhao, Y. Zhang, Y. Xiao, and W. Liu, Exact two-component relativistic energy band theory and application, *J. Chem. Phys.* **144**, 044105 (2016).
- [2] J. C. Slater, A simplification of the Hartree–Fock method, *Phys. Rev.* **81**, 385 (1951).
- [3] S. H. Vosko, L. Wilk, and M. Nusair, Accurate spin-dependent electron liquid correlation energies for local spin density calculations: a critical analysis, *Can. J. Phys.* **58**, 1200 (1980).
- [4] J. P. Perdew, K. Burke, and M. Ernzerhof, Generalized Gradient Approximation Made Simple, *Phys. Rev. Lett.* **77**, 3865 (1996).
- [5] J. P. Perdew, A. Ruzsinszky, G. I. Csonka, O. A. Vydrov, G. E. Scuseria, L. A. Constantin, X. Zhou, and K. Burke, Restoring the Density-Gradient Expansion for Exchange in Solids and Surfaces, *Phys. Rev. Lett.* **100**, 136406 (2008).
- [6] J. Tao, J. P. Perdew, V. N. Staroverov, and G. E. Scuseria, Climbing the Density Functional Ladder: Nonempirical Meta–Generalized Gradient Approximation Designed for Molecules and Solids, *Phys. Rev. Lett.* **91**, 146401 (2003).
- [7] J. P. Perdew, A. Ruzsinszky, G. I. Csonka, L. A. Constantin, and J. Sun, Workhorse Semilocal Density Functional for Condensed Matter Physics and Quantum Chemistry, *Phys. Rev. Lett.* **103**, 026403 (2009).
- [8] J. P. Perdew, A. Ruzsinszky, G. I. Csonka, L. A. Constantin, and J. Sun, Erratum: Workhorse Semilocal Density Functional for Condensed Matter Physics and Quantum Chemistry [*Phys. Rev. Lett.* 103, 026403 (2009)], *Phys. Rev. Lett.* **106**, 179902 (2011).
- [9] J. Tao and Y. Mo, Accurate Semilocal Density Functional for Condensed-Matter Physics and Quantum Chemistry, *Phys. Rev. Lett.* **117**, 073001 (2016).
- [10] J. P. Perdew, S. Kurth, A. Zupan, and P. Blaha, Accurate Density Functional with Correct Formal Properties: A Step Beyond the Generalized Gradient Approximation, *Phys. Rev. Lett.* **82**, 2544 (1999).
- [11] J. W. Furness, A. D. Kaplan, J. Ning, J. P. Perdew, and J. Sun, Accurate and numerically efficient  $r^2$ SCAN meta-generalized gradient approximation, *J. Phys. Chem. Lett.* **11**, 8208 (2020).
- [12] J. W. Furness, A. D. Kaplan, J. Ning, J. P. Perdew, and J. Sun, Correction to “Accurate and numerically efficient  $r^2$ SCAN meta-generalized gradient approximation”, *J. Phys. Chem. Lett.* **11**, 9248 (2020).

- [13] M. A. L. Marques, M. J. T. Oliveira, and T. Burnus, LIBXC: A library of exchange and correlation functionals for density functional theory, *Comput. Phys. Commun.* **183**, 2272 (2012).
- [14] S. Lehtola, C. Steigemann, M. J. T. Oliveira, and M. A. L. Marques, Recent developments in LIBXC – a comprehensive library of functionals for density functional theory, *SoftwareX* **7**, 1 (2018).
- [15] LIBXC, Version 6.0.0, available from <https://www.tddft.org/programs/libxc/> (retrieved August 16, 2022).
- [16] F. Weigend and A. Baldes, Segmented contracted basis sets for one- and two-component Dirac–Fock effective core potentials, *J. Chem. Phys.* **133**, 174102 (2010).
- [17] S. Grimme, J. Antony, S. Ehrlich, and H. Krieg, A consistent and accurate ab initio parametrization of density functional dispersion correction (DFT-D) for the 94 elements H–Pu, *J. Chem. Phys.* **132**, 154104 (2010).
- [18] S. Grimme, S. Ehrlich, and L. Goerigk, Effect of the damping function in dispersion corrected density functional theory, *J. Comput. Chem.* **32**, 1456 (2011).
- [19] C. R. Berry, Physical defects in silver halides, *Phys. Rev.* **97**, 676 (1955).
- [20] P. Wang, B. Huang, X. Zhang, X. Qin, H. Jin, Y. Dai, Z. Wang, J. Wei, J. Zhan, S. Wang, J. Wang, and M.-H. Whangbo, Highly efficient visible-light plasmonic photocatalyst Ag@AgBr, *Chem. Eur. J.* **15**, 1821 (2009).
- [21] G. Piermarini and C. Weir, A diamond cell for X-ray diffraction studies at high pressures, *J. Res. Natl. Bur. Stan., Sec. A* **66**, 325 (1962).
- [22] R. Łazarski, A. M. Burow, L. Grajciar, and M. Sierka, Density functional theory for molecular and periodic systems using density fitting and continuous fast multipole method: Analytical gradients, *J. Comput. Chem.* **37**, 2518 (2016).
- [23] M. Becker and M. Sierka, Density functional theory for molecular and periodic systems using density fitting and continuous fast multipole method: Stress tensor, *J. Comput. Chem.* **40**, 2563 (2019).
- [24] G. Kresse and J. Furthmüller, Efficiency of ab-initio total energy calculations for metals and semiconductors using a plane-wave basis set, *Comput. Mater. Sci.* **6**, 15 (1996).
- [25] R. Ahlrichs, M. Bär, M. Häser, H. Horn, and C. Kölmel, Electronic structure calculations on workstation computers: The program system turbomole, *Chem. Phys. Lett.* **162**, 165 (1989).
- [26] Developers’ version of TURBOMOLE V7.7 (2022), a development of University of Karlsruhe and Forschungszentrum Karlsruhe GmbH, 1989-2007, TURBOMOLE GmbH, since 2007;

available from <https://www.turbomole.org> (retrieved May 4, 2023).

- [27] Manual of TURBOMOLE V7.7 (2022), a development of University of Karlsruhe and Forschungszentrum Karlsruhe GmbH, 1989-2007, TURBOMOLE GmbH, since 2007; available from <https://www.turbomole.org/turbomole/turbomole-documentation/> (retrieved May 4, 2023).